DEPARTAMENT OF MATERIALS SCIENCE

MANUEL RENATO FERREIRA ALVES DE MACEDO BSc in Materials Engineering

Development and Evaluation of Scaffolds for Bone Regeneration,

Produced by 3D Printing and coated with a composite of PCL and Bioglass® Doped with Magnesium

MASTER IN MATERIALS ENGINEERING
NOVA University Lisbon
September, 2024



DEPARTAMENT OF MATERIALS SCIENCE

Development and Evaluation of Scaffolds for Bone Regeneration,

Produced by 3D Printing and coated with a composite of PCL and Bioglass® Doped with Magnesium

MANUEL RENATO FERREIRA ALVES DE MACEDO

BSc in Materials Engineering

Adviser: Jorge Carvalho Silva

Associate Professor, NOVA University Lisbon

Co-advisers: Ana Sofia Pádua

PhD student, NOVA University Lisbon

Examination Committee:

Chair: Alexandre Velhinho,

Assistant Professor, NOVA University Lisbon

Rapporteurs: João Paulo Borges,

Full Professor, NOVA University Lisbon

Adviser: Jorge Carvalho Silva,

Associate Professor, NOVA University Lisbon

Members:

Development and Evaluation of Scaffolds for Bone Regeneration, produced by 3D Printing and coated with a composite of PCL and Bioglass® Doped with Magnesium
Copyright © Manuel Macedo, NOVA School of Science and Technology, NOVA University Lisbon.
The NOVA School of Science and Technology and the NOVA University Lisbon have the right, perpetual and without geographical boundaries, to file and publish this dissertation through printed copies reproduced on paper or on digital form, or by any other means known or that may be invented, and to disseminate through scientific repositories and admit its copying and distribution for non-commercial, educational or research purposes, as long as credit is given

to the author and editor.



ACKNOWLEDGMENTS

Gostaria de expressar a minha mais profunda gratidão aos meus pais e a minha família, que me acompanharam não só em todo o percurso académico, mas também em cada etapa da minha vida, sempre disponíveis para oferecer o seu amor, apoio e incentivo, sabendo como tirar o melhor de mim. Aos meus amigos de infância, pela amizade duradoura e por saber que posso sempre contar com eles. Aos amigos que fiz mais recentemente na faculdade, pela camaradagem e pelas longas horas de estudo que partilhámos, que tornaram o curso muito menos cansativo. Um agradecimento especial à minha namorada pelo apoio incondicional e pela paciência durante as inúmeras horas que passou à minha espera enquanto eu estava no laboratório.

Quero também agradecer a esta grandiosa Faculdade de Ciências e Tecnologias da Universidade Nova de Lisboa por me ter proporcionado cinco anos incríveis. Em particular, deixo o meu reconhecimento ao meu departamento, o DCM, ao seu presidente, Prof. Dr. João Paulo Borges, ao coordenador do curso, Prof. Dr. Alexandre Velhinho, e a todas as pessoas que o representam, pela amabilidade e apoio ao longo desta jornada. Gostaria também de agradecer ao Sr. Afonso Moutinho e ao Sr. Bruno Costa, do DF, pela ajuda e tempo gasto aprendizagem da técnica de impressão 3D.

Ao Prof. Dr. Jorge Silva, agradeço a oportunidade e apoio em dois projetos, permitindome aprender e crescer de forma significativa. Agradeço igualmente aos meus colegas do laboratório de Engenharia de Tecidos, que estiveram sempre prontos a ajudar quando necessário e contribuíram para um ambiente de trabalho acolhedor e colaborativo. O meu mais sincero agradecimento vai para a minha coorientadora Ana Sofia Pádua e para a Dra. Tânia Vieira, que foi minha coorientadora no Projeto de Licenciatura, duas pessoas incríveis que generosamente disponibilizaram o seu tempo para me ajudar, assim como a muitos outros.

Para concluir, deixo o meu mais sincero agradecimento a todos que, de alguma forma, contribuíram para o meu crescimento pessoal e académico ao longo desta jornada. Sem o vosso apoio incondicional, orientação e companhia, nada disso teria sido possível. Obrigado.

"The moment you give up is the moment you let someone else win."

By Kobe Bryant.

ABSTRACT

Bone regeneration is currently one of the most prominent areas in tissue engineering, particularly in the treatment of critical size defects, where the bone's natural healing capacity is insufficient. The use of biodegradable scaffolds offers promising solutions by mimicking the extracellular matrix and providing a strong scaffold for bone growth.

This study investigates the creation and performance of bioactive scaffolds for bone regeneration using polylactic acid (PLA) coated with a polycaprolactone (PCL) composite incorporating magnesium-doped bioglass (Mg-BG). The Fused Deposition Modelling (FDM) technique was used to create the scaffolds, with an emphasis on bioactivity and cellular interaction.

The chemical composition of the coating was analysed using Fourier transform infrared spectroscopy (FTIR), while the surface morphology was evaluated using scanning electron microscopy (SEM) and energy dispersive spectroscopy (EDS). The release of ions from the compound was evaluated using inductively coupled plasma (ICP) spectroscopy. The scaffolds were also tested for bioactivity through immersion in simulated body fluid (SBF) and the formation of an apatite layer was monitored over a period of 14 days. Cytotoxicity and cell proliferation were evaluated through resazurin assays in human osteosarcoma cells (SaOS-2), while cellular activity was measured by the release of ALP (alkaline phosphatase).

The results revealed that magnesium-doped bioglass composites demonstrated improved bioactivity, more stable ion release, greater cell adhesion and proliferation, and lower cytotoxicity compared to undoped bioglass, exhibiting their potential for osteogenic applications. These data suggest that Mg-doped bioglass is a notable option for bone tissue engineering applications, offering essential bioactive properties to improve bone regeneration.

Keywords: Tissue Engineering, Additive Manufacturing, Composite, Doped-Bioglass®

RESUMO

A regeneração óssea é atualmente uma das áreas de maior destaque na engenharia de tecidos, particularmente no tratamento de defeitos de tamanho crítico, onde a capacidade de cicatrização natural do osso é insuficiente. A utilização de *scaffolds* biodegradáveis oferece soluções promissoras ao imitar a matriz extracelular e fornecer uma estrutura fortalece para o crescimento ósseo.

Este estudo investiga a criação e o desempenho de scaffolds bioativos, para regeneração óssea, utilizando poliácido lático (PLA), revestido com um compósito de policaprolactona (PCL) incorporando biovidro dopado com magnésio (Mg-BG). Foi utilizada a técnica de Modelação por Deposição Fundida (FDM) para a criação dos scaffolds, com ênfase na bioatividade e interação celular.

A composição química do revestimento foi analisada através de espectroscopia de infravermelho por transformada de Fourier (FTIR), enquanto a morfologia superficial foi avaliada utilizando microscopia eletrónica de varrimento (SEM) e espectroscopia de dispersão de energia (EDS). A libertação de iões do composto foi avaliada através de espectroscopia de plasma indutivamente acoplado (ICP). Os scaffolds foram ainda testados quanto à bioatividade, através da imersão em fluido corporal simulado (SBF) e foi monitorizada da formação de camada de apatite ao longo de um período de 14 dias. A citotoxicidade e a proliferação celular foram avaliadas através de ensaios de resazurina em células humanas de osteossarcoma (SaOS-2), enquanto a atividade celular foi medida pela libertação de fosfatase alcalina ALP.

Os resultados revelaram que os compósitos de biovidro dopados com magnésio demonstraram bioatividade melhorada, libertação de iões mais estável, maior adesão celular e proliferação e menor citotoxicidade em comparação com o biovidro não dopado, exibindo o seu potencial para aplicações osteogénicas. Estes dados sugerem que os biovidro dopado com Mg é uma opção notável para as aplicações em engenharia de tecidos ósseos, oferecendo propriedades bioativas essenciais para melhorar a regeneração óssea.

Keywords: Engenharia de Tecidos, Impressão 3D, Compósito, Biovidro® Dopado

CONTENTS

1	INTE	RODUCTION	1
	1.1	The bone	1
	1.1.1	Bone healing process	1
	1.2	Defects treatment	2
	1.3	Bone tissue engineering	4
	1.3.1	Scaffold production	4
2	Ma	TERIALS AND METHODS	7
	2.1	Structure production	7
	2.2	ATR-FTIR	7
	2.3	SEM-EDS	7
	2.4	Inductively Coupled Plasma (ICP) - Atomic Emission Spectroscopy	8
	2.5	Bioactivity	8
	2.6	Cell Study	8
	2.6.1	Adhesion and proliferation	9
	2.6.2	Alkaline Phosphatase activity	9
	2.6.3	Cell morphology and spreading characterization: DAPI and Phalloidin Labelling	J.9
3	Res	JLTS AND DISCUSSION	.11
	3.1	Results	11
	3.1.1	ATR-FTIR	11
	3.1.2	SEM-EDS	.13

4	CONC	THISION AND FITTURE PERSPECTIVES	20
	3.2	Discussion	26
	3.1.6	Cell Adhesion and Proliferation	22
	3.1.5	Cytotoxicity	21
	3.1.4	Bioactivity	19
	3.1.3	Inductively Coupled Plasma (ICP) - Atomic Emission Spectroscopy	17

LIST OF FIGURES

Figure 1.1 - Bone tissue and cells generated substances	2
Figure 1.2 - Different concepts for Bone regenerative fixation or scaffolding	3
Figure 1.3 - Different bone fixating devices	5
Figure 1.4 - Different 3D printing technologies	6
Figure 3.1 - BG and doped BG's Fourier Transform Infrared Spectroscopy analysis	12
Figure 3.2 - PCL's Fourier Transform Infrared Spectroscopy analysis	12
Figure 3.3 - PCL/BG composite's Fourier Transform Infrared Spectroscopy analysis	13
Figure 3.4 - SEM images of BG powder and doped BG powder	14
Figure 3.5 - Lognormal particle size distribution of BG and doped BG	15
Figure 3.6 - EDS images of BGand doped BG	17
Figure 3.7 - Ca, P, Si, Na and Mg Ion released from ICP test results	18
Figure 3.8 - Cytotoxicity assessment of PCL and PCL/BG composites	21
Figure 3.9 - Cell adhesion and proliferation of SaOs-2 on PCL and PCL/BG composites	22
Figure 3.10- Cell activity of SaOs-2 on PCL and PCL/BG composites	23
Figure A.1 - 3D model of the structure for cell-based tests	39
Figure A.2 - Printed structures for cell-based tests	39
Figure A.3 - Printed structures for cell-based tests with coating	40

LIST OF TABLES

Table 3.1 - Parameters of the lognormal particle size distributions	16
Table 3.2 - Si, P, O, Ca, Na and Mg atomic percentages	16
Table 3.3 - SEM Images of PCL/BG apatite layer formation	19
Table 3.4 - Ca, Na, P, Si and Mg atomic percentage at film's surface, by EDS Imaging	20
Table 3.5 - Proliferation of SaOs-2 cells on each material	23
Table 3.6 - DAPI fluorescence staining images	24

GLOSSARY

Additive A process that builds up an object by adding material layer by layer, typi-

Manufacturing cally called 3D printing. Objects are based of digital models.

Apatite The process of calcium and phosphate ion deposition on the surface of a

Formation scaffold, mimicking natural bone mineralization.

Bioactive The quality of a material that interacts with biological tissue in a way that

promotes biological progress.

Biocompatibil- The ability of a material to interact with biological systems without eliciting

ity an adverse reaction.

Biodegradable Refers to materials that break down over time within the body through

natural processes.

Biomaterial Any material, synthetic or natural, that is used to interact with biological

systems for medical purposes.

Bioresorbable A material that is not only biodegradable but is also absorbed and metab-

olized by the body over time.

Bone The process by which osteoclasts break down bone tissue, releasing min-

Resorption erals into the bloodstream.

Cytokines Small proteins that are crucial in cell signalling.

Cytotoxicity The quality of being toxic to cells.

Hydrolytic The process in which a material degrades by reaction with water.

Degradation

Osteoblasts Bone-forming cells responsible for synthesizing bone matrix and facilitat-

ing mineralization.

Osteoclasts Cells that break down bone tissue by resorbing the bone matrix.

Osteoconduc- The ability of a material to serve as a scaffold for new bone growth.

tivity

Osteogenesis The process of new bone formation

Osteoinductiv- The ability of a material to stimulate undifferentiated cells to develop into

ity bone-forming cells, promoting new bone formation.

Scaffolds Structures designed to support cell growth and tissue regeneration.

Tissue A multidisciplinary field that combines biology, engineering, and material

Engineering science to develop functional substitutes for damaged tissues and organs.

ACRONYMS

ECM Extra cellular matrix.

MSC Mesenchymal Stem Cells.

BTE Bone tissue engineering

PLA Polylactic acid

PCL Polycaprolactone

BG Bioglass[®]

DBG Doped Bioglass[®]

ALP Alkaline Phosphatase

FDM Fused Deposition Modelling

SLA Stereolithography

SLS Selective Laser Sintering

DLP Digital Light Processing

ATR-FTIR Attenuated Total Reflectance Fourier-Transform Infrared spectroscopy

SEM Scanning Electron Microscopy

EDS Energy dispersive X-ray Spectroscopy

ICP Inductively Coupled Plasma

PBS Phosphate-buffered Saline

SBF Simulated Body Fluid

SaOs-2 Sarcoma Osteogenic cell line

DAPI 4',6-diamidino-2-phenylindole

SYMBOLS

Location parameter of a lognormal distribution. It is equivalent to the mean of the normal distribution of the logarithmic values.
 β Scale parameter of a lognormal distribution. It is equivalent to the standard deviation of the normal distribution of the logarithmic values.
 Med(X) The median of a distribution is the value at which 50% of the distribution lies below and 50% lies above.
 μ The mean of the log-normal distribution is the probability-weighted average of all possible values.
 Mod(X) The mode is the global maximum of the distribution.

persion of the data.

The standard deviation of a distribution is a measure of the spread or dis-

Measure of the acidity or alkalinity of a solution.

рΗ

σ

INTRODUCTION

1.1 The bone

Bone serves as the body's framework, providing structural, mechanical, and physiological functions. It offers protection to vital organs, such as the brain and lungs, within the cranial and thoracic cavities. Bone structure is essential for movement, by supporting muscles and connecting to them through joints to enable unique types of movement.[1] - [4] Bone also serves as a reservoir for essential minerals like calcium and phosphorus, crucial for homeostasis. It's vital for haematopoiesis, producing and storing blood stem cells that differentiate into red blood cells, white blood cells, and platelets.[1] - [3]

The natural bone Extra-Cellular Matrix (ECM) is composed of organic and inorganic components, that provide mechanical support and facilitate cellular functions.[1] - [7] Collagen is a fibrous protein and the biggest organic component that bone presents, offering flexibility and tensile strength to it, allowing the withstand of mechanical stresses and deformations.[2] - [6] Hydroxyapatite is a mineralized form of calcium phosphate and confers rigidity and compressive strength to the bone while being bioactive, promoting cell adhesion, proliferation, and differentiation.[2] - [8] Thus, an ideal scaffold must imitate the ECM's morphological and mechanical properties.

1.1.1 Bone healing process

In order to construct structures able to help bone healing, we must comprehend bone's regenerative capabilities and its constituents. Bone healing is essential for maintaining skeletal integrity, development, and continuous remodelling through its lifetime. This process involves cellular and molecular mechanisms, as depicted in Figure 1.1, indispensable for healing

fractures and repairing defects. Bone cells (osteoblasts and osteoclasts), signalling system (eg. growth factors) and the ECM are the main components responsible for this task.[9] Osteoblasts originate from Mesenchymal Stem Cells (MSC), normally stored in the bone marrow.[10] - [12] When a fracture occurs, MSC's are stimulated by cytokines to proliferate, concentrate, and differentiate at the fracture site.[2] - [7], [12] Differentiated osteoblasts secrete type-I collagen forming a non-mineralized fibrous matrix.[7], [11] The vascular ingrowth process ensures the transport of nutrients and oxygen to new tissue and matrix mineralization, starting ECM formation.[11] The final pass of the bone healing process Is bone remodelling phase, where osteoclasts and osteoblasts communicate via cytokines to regulate bone growth and remodelling. Unlike other tissues healing process, this one normally doesn't exhibit any scars and largely recovers all the organ's pre-injury properties. [5], [12]

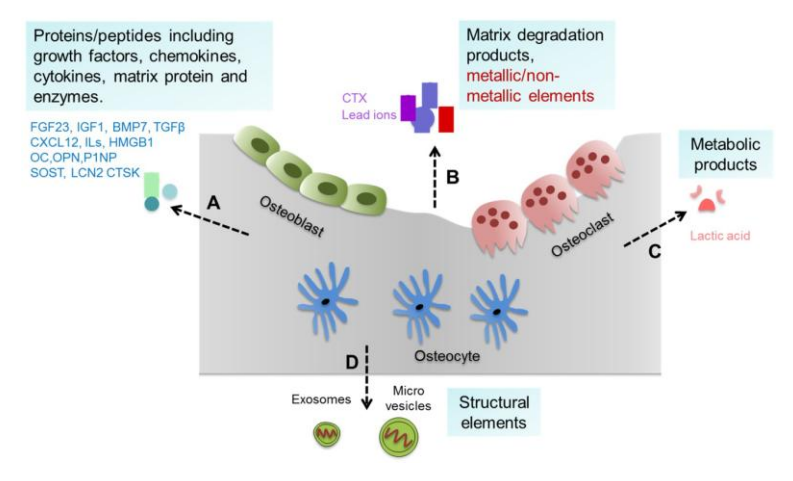


Figure 1.1 - Bone tissue and cells generated substances: (A) Proteins/peptides including growth factors, cytokines and enzymes. (B) Matrix degradation products such as CTX and lead ions. (C) Metabolic products of bone cells such as lactic acid. (D) Structural elements secreted by bone cells. [1]

1.2 Defects treatment

Despite our organism ability to maintain structural stability through bone's regenerative ability, defects exceeding 2 cm surpass the critical size threshold, requiring the assistance of supportive structures. These defects may arise from trauma, fracture, tumour, infection, genetic abnormalities or metabolic disorders, and compromising ECM's structural integrity.[12] - [20] For the last 7 years there has been around 20 to 30 million orthopedic surgeries taking place annually, being the second most transplanted tissue worldwide. [21]

Figure 1.2 presents a variety of strategies, with the selection of each one depending on the specific type of bone defect. Per example, bone grafts involve transplanting healthy bone fragments to the defect site. Allografts use donor fragments, while autografts use the patient's own bone, avoiding rejection but requiring more surgeries. These types of treatment are normally used in defects caused by a disease.[14] - [20], [22] - [24]

For traumas and fractures, metal screws and plates, (internal fixation devices) help grip the bone together while it heals. Typically made of stainless steel or titanium, they may need to be removed afterward, in cases of younger patients or when the device causes discomfort, requiring subsequent operations. [18], [19], [24], [25]

According to the Alvarez and Nakajima (2009)[18], orthopedic procedures in the US have a 5% infection risk, leading to 100,000 infections annually. These infections result from bacterial colonization and biofilm formation on the device's surface. Components wear may result in micro and nanoparticles deemed foreign by our organisms and can cause chronic inflammation. Stress shielding is caused when the implant disrupts the bone's natural load distribution, leading to bone loss and weakening from reduced mechanical stimulation. These effects can affect the implant's long-term stability and regeneration.[24] - [26]

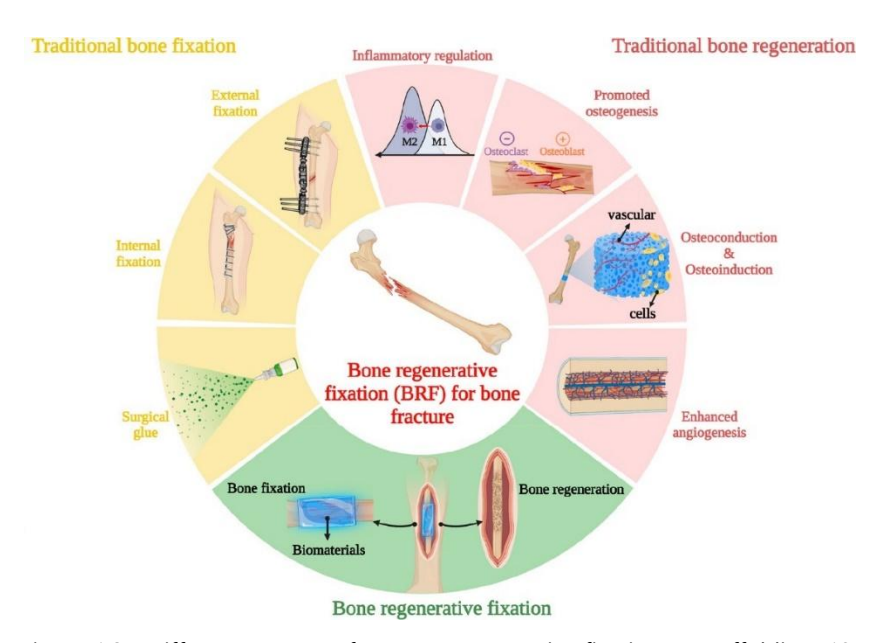


Figure 1.2 - Different concepts for Bone regenerative fixation or scaffolding.[19]

Recent progress in tissue engineering focuses on replacing metal support structures with biodegradable ones to treat bone defects. This approach offers benefits like less wear, fewer surgeries due to material biodegradation, and faster regeneration through dopant materials and biomolecular signals.[24], [25]

1.3 Bone tissue engineering

Bone tissue engineering (BTE) focus on new techniques for bone regeneration exploring alternative material and technologies to treat damaged or deceased tissue. Some of the technologies being explored include the use of biomaterials, cell-based strategies and growth factors.[27] - [33] Cell-seeding technology consists *in vitro* manipulation of stem cells that differentiate into bone forming cells and injecting them in affected areas, while growth factors stimulate osteoblasts proliferation at the damaged site.[32] - [34] However, the most investigated structures are supportive scaffolds produced with biomaterials that provide a temporary framework mimicking bone's extracellular matrix. The structure also promotes osteogenic cell attachment, proliferation, and differentiation. Furthermore, both the first technologies can be included in the scaffolds production, to enhance their properties for bone treatment.[27] - [34]

1.3.1 Scaffold production

Advanced scaffold production is a key component of BTE, requiring knowledge of materials science, biology, and engineering. The ideal scaffolds should mimic the bone's natural environment, providing mechanical support and enhancing regeneration.[27] - [30]

Biodegradable scaffolds garnered considerable interest as they facilitate gradual tissue replacement. Material choice is crucial, as it must balance biocompatibility, biodegradability, mechanical properties, and manufacturability. Common materials include natural polymers (collagen, chitosan), synthetic polymers (PLA, PCL), and bioactive ceramics.[27] - [30] Production methods also play a significant role in determining the scaffold's properties. Techniques such as solvent casting, gas foaming, freeze-drying, electrospinning, and 3D printing have been employed, each with its own advantages and limitations.[27] - [30]

1.3.1.1 Materials in scaffold production

The materials used for the scaffold production normally depend on the method, as some materials are incompatible with certain production methods. Nevertheless, each material has unique characteristics beneficial for bone healing.

Metal-based scaffolds, or fixation implants, are the most used structures to support bone healing. Metal plates and screws, typically made from stainless steel or titanium alloys, help fix fractured bones. Stainless steel is rigid and corrosion-resistant, while titanium alloys are lighter and more flexible, reducing stress shielding but are more expensive. Joint replacements, as depicted in Figure 1.3, are prosthetic devices typically made from inert metals that often incorporate ceramic and plastic components.[18]

Ceramics are rarely used for implants and scaffolds due to their brittleness, making them unsuitable for support structures. However, ceramics like tricalcium phosphate and bioactive glass have high interest in BTE due to their resemblance to bone minerals and ability to bond the scaffold to the ECM.[34] - [37]

Polymeric materials such as PLA, and PCL offer various benefits and disadvantages, compared with metallic scaffolds. Their low stiffness makes them less effective for supportive roles but also reduces the likelihood of stress shielding.[25], [27], [30] Unlike metals, biodegradable polymers break down gradually and disappear after the wound heals, reducing the need for extra surgeries and long-term discomfort. Different polymers with varying degradation rates can be chosen to match the bone healing process, providing consistent support.[30], [39]

To improve polymers mechanical disadvantages, ceramic and even metallic powder reinforcements can be mixed with the polymer to achieve the desired properties and culminate in a better biomaterial for bone scaffold production.[40] - [42]. Polymers like those mentioned earlier can substitute collagen in scaffold production, which should also be bioactive to stimulate new bone formation and integration.[34], [37], [41]

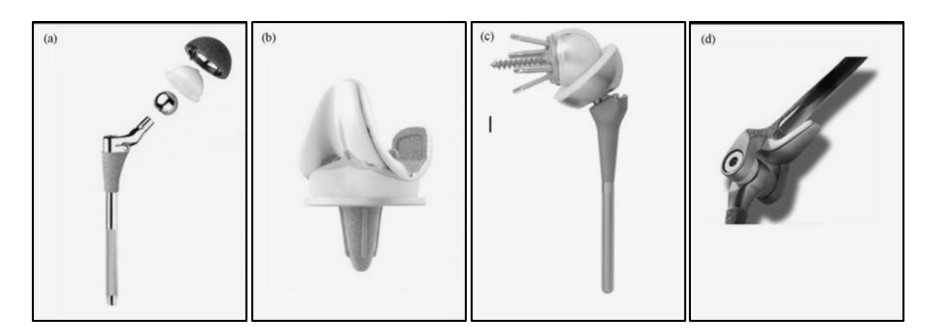


Figure 1.3 - Different bone fixating devices using metallic, ceramic and plastic parts. Hip(a), knee(b), shoulder(c) and elbow(d) prosthetics.[79]

Including Bioglass® 45S5 (45% SiO₂, 24.5% CaO, 24.5% Na₂O, and 6.0% P₂O₅ in wt.%) in this framework, provides some rigidity while promoting osteoconductivity. BG has the ability to bond with the ECM, creating a hydroxyapatite layer that promotes cell attachment and proliferation.[40] - [42] Furthermore, BG releases ions, such as Si, Ca, and P, triggering cellular

responses that encourage bone regeneration. The high concentration of ions leads to an anti-bacterial effect due to pH changes, although they may reduce cellular adhesion. The synergy between these two is very promising for tissue engineering and bone regeneration. [43] - [49] Magnesium (Mg) is a very important mineral in the ECM, and its presence will improve the ceramic's bioactive properties. When doping BG with magnesium, it acts as a network modifier, breaking Si–O–Si bonds and introducing non-bridging oxygens. This alters the BG properties, improving stability, degradation rate, and bioactivity. [43] - [48]

1.3.1.2 Techniques in scaffold production

Additive manufacturing offers precise control over scaffold architecture, though material exploration continues. Various 3D printing technologies (Figure 1.4) can transform digital designs into physical scaffolds.

Stereolithography (SLA) and Digital Light Processing (DLP) use UV light to harden resin, while Selective Laser Sintering (SLS) fuses powdered materials like metals, polymers, and ceramics with a high-intensity laser.[50] - [59] Fused Deposition Modelling (FDM) melts and extrudes plastic filament layer by layer and is preferred for its cost-effectiveness and compatibility with low-melting polymers.[60] - [65] This study focuses on PLA scaffolds produced via FDM, coated with a PCL and doped BG composite.

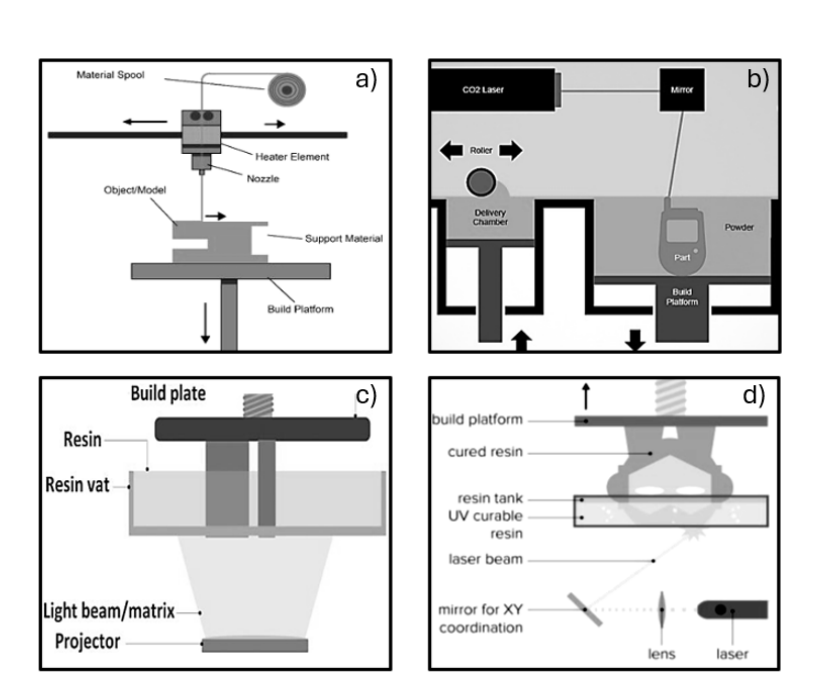


Figure 1.4 - Different 3D printing technologies; a) Fused Deposition Modelling [80]; b) Selective Laser Sintering [50]; c) Digital Light Processing [58]; d) Stereolithography [58]

MATERIALS AND METHODS

2.1 Structure production

In this study, FDM technology was used to fabricate structures and then coated with a PCL-based composite film containing Mg-doped BG powder. Structures were designed in Autodesk Fusion Pro and processed to generate a G-code for the Original Prusa MK4 printer. They had a 1 cm 2 surface area, a wall to hold 500 μ l, a 15.8 mm base diameter, and a rough surface to simulate bone texture. The images of the structures are provided in Appendix A.

The structures were coated with a solution of chloroform (Carlo Erba, cas 43861), PCL (gifted), and BG produced according Gavinho, *et al.* (2023) [41]. Five solutions were prepared with 85% chloroform and 15% of either pure PCL or a PCL and BG mix (2:1 or 4:1 ratio), with both doped and undoped BG. Finally, the coated structures were heat-treated at 85°C for 20 minutes.

2.2 ATR-FTIR

Chemical characterization was performed using attenuated total reflectance Fourier-transform infrared spectroscopy with a PerkinElmer spectrometer. This technique measures the infrared absorption of chemical bonds in the molecules. Spectra were recorded from 4000 to 400 cm⁻¹ with a 1 cm⁻¹ resolution step size.

2.3 SEM-EDS

BG and doped-BG powders were imaged using a Hitachi SU8200 SEM with a 20 nm gold-palladium coating (Quorum Q300T D). The imaging conditions were 5 kV acceleration voltage, 8.3 mm working distance, 500x magnification. EDS images were taken with an Oxford INCA

Energy 350 detector. For bioactivity testing, films were examined with a Hitachi TM3030Plus microscope, coated with 35 nm gold-palladium (Quorum Q150t ES). The imaging conditions were 15 kV acceleration voltage, 8.2 mm working distance, 500x magnification. EDS data were collected using a Bruker QUANTAX - XFlash® 7 Series detector.

2.4 Inductively Coupled Plasma (ICP) - Atomic Emission Spectroscopy

The Horiba Jobin-Yvon Ultima was used for ICP tests. Each film (300 mg) was submerged in 6 ml of PBS (50 mg/ml). Measurements were taken at 0, 24, and 48 hours to monitor changes.

2.5 Bioactivity

It's crucial these materials remain intact until bone regeneration is complete. We also need to determine if BG and Mg-doped BG affect the composite degradation rate. To assess this, scaffolds were submerged in Simulated Body Fluid (SBF) at 37°C, following Kokubo, *et al.* (1990)[66] Samples were analysed by SEM and EDS at 0, 3, 7, and 14 days to characterize degradation and apatite layer formation.

2.6 Cell Study

The SaOS-2 osteosarcoma cell line was used for cytotoxicity, adhesion, proliferation, and ALP activity assays. Cells were cultured in McCoy 5A Medium (Sigma-Aldrich®) at 37° C in 5% CO₂. Cells were then trypsinized with 0.25% trypsin and resuspended in the medium. For cytotoxicity assays, cells were seeded into 96-well plates at 3×10^{4} cells/cm², and for adhesion, proliferation, and ALP activity assays, into 24-well plates at 2×10^{4} cells/cm².

2.6.1 Cytotoxicity

Cytotoxicity assays exposed SaOs-2 to a medium in contact with PCL and BG films substrate to check for toxicity. Each experiment included a positive control (0.1% Triton), a negative control (culture medium), and various concentrations (25, 50, 100 mg/ml) of PCL and BG films. The films were incubated for 48 hours, with four samples per film tested. Cell viability and cytotoxicity were assessed using the resazurin assay.

2.6.2 Adhesion and proliferation

Resazurin ($C_{12}H_7NO_4$), a blue solution, is reduced to pink resorufin ($C_{12}H_7O_3$) by the NAD enzyme from metabolically active cells, indicating cell viability. The colour change intensity is proportional to the number of living cells. Absorbance was measured at 601 nm and 571 nm from a 50% v/v resazurin solution mixed with McCoy medium, incubated with cells for 3 hours. The resazurin solution (Alfa Aesar®) was prepared in PBS at 0.04 mg/ml. Tests were conducted on days 1, 3, 7, 10, and 14 post-seeding to monitor proliferation

2.6.3 Alkaline Phosphatase activity

Alkaline phosphatase (ALP), an enzyme marker for osteogenesis, was assessed using a colorimetric assay.[4], [30] A 1 mg/ml solution of 4-nitrophenyl phosphate disodium salt in tris-HCl buffer (pH 8.7) was prepared. The medium in contact with samples was filtered to remove debris, and baseline absorbance was measured at 405 nm. The ALP solution was mixed with the medium (1:1) and incubated for 20 minutes, then absorbance was measured again at 405 nm. Results were normalized to the cell population from the previous day.

2.6.4 Cell morphology and spreading characterization: nucleus and cytoskeleton labelling

Cells adherent from the resazurin tests at days 7 and 14 were washed with PBS (pH 7.4) and fixed with 4% paraformaldehyde (Santa Cruz Biotechnology®) for 20 minutes at room temperature. Cell membranes were permeabilized with 0.1% Triton (Sigma-Aldrich®) in PBS, then stained with 0.1% Phalloidin CruzFluorTM 488 (Santa Cruz Biotechnology®) for 90 minutes in the dark. They were then stained with 100 μ L of 33 μ g/mL DAPI in PBS for 5 minutes in a dark room. Each step included three PBS rinses and a final rinse with distilled water.

Samples were mounted on glass slides with 10 μ L of Mowiol (Sigma-Aldrich®) and observed under optical microscopy (Nikon Eclipse Ti-S) at 100x and 400x magnification, using excitation wavelengths of 494 nm for phalloidin and 350 nm for DAPI. Images were processed with ImageJ."

RESULTS AND DISCUSSION

3.1 Results

3.1.1 ATR-FTIR

and 1480-1410 cm⁻¹, corresponding to C-H stretching vibrations and CO₃²⁻ groups. As BG lacks carbon and hydrogen, the C-H bands likely stem from isopropanol used for cleaning, while CO₃²⁻ bands result from atmospheric CO₂ reacting with non-bridging oxygens. [41] Bioglass, an amorphous ceramic with a disordered network of phosphorous, silicon, and oxygen ions, has unbonded sites that attract dipole molecules like H₂O and react with CO₂. Magnesium doping increases structural instability as a network modifier, described by Sergi, et al. (2020) [41], and evident from the higher intensity of impurity peaks in the spectra. The characteristic peaks of BG are observed between 1200 and 400 cm⁻¹. Within this range, Si-O-Si stretching and bending vibrations are identified at 1015 cm⁻¹ and 667 cm⁻¹, respectively, while Si-O stretching of non-bridging oxygens occurs at 905 cm⁻¹.[67], [68] Additionally, the shoulder at 867 cm⁻¹ and peaks at 730 cm⁻¹ and 712 cm⁻¹ are typically linked to P-O-P and P-O stretching, with the latter also associated with CO₃²⁻ bending. The final peak, located at 590 cm⁻¹, corresponds to asymmetric vibrations of PO₄³⁻.[42], [67], [68] The FTIR analysis of PCL (Figure 3.2) showed peaks at 2945 cm⁻¹ and 2866 cm⁻¹ for asymmetric and symmetric C-H stretching, 1722 cm⁻¹ for C=O stretching, and 1239 cm⁻¹ and 1163 cm⁻¹ for symmetric and asymmetric C-O-C stretches.[28], [41], [69] - [72]

The BG's FTIR analysis, from the graphs in Figure 3.1, showed bands between 2990-2900 cm⁻¹

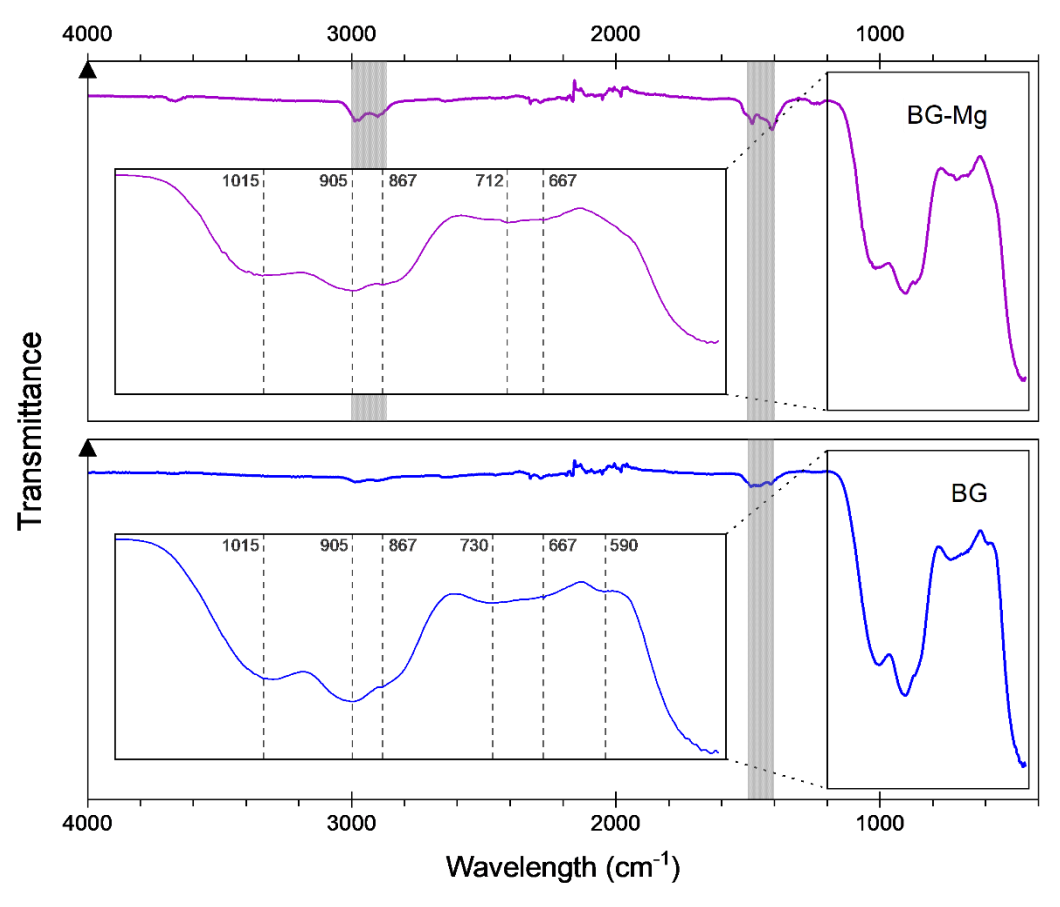


Figure 3.2 - BG and doped BG's Fourier Transform Infrared Spectroscopy analysis

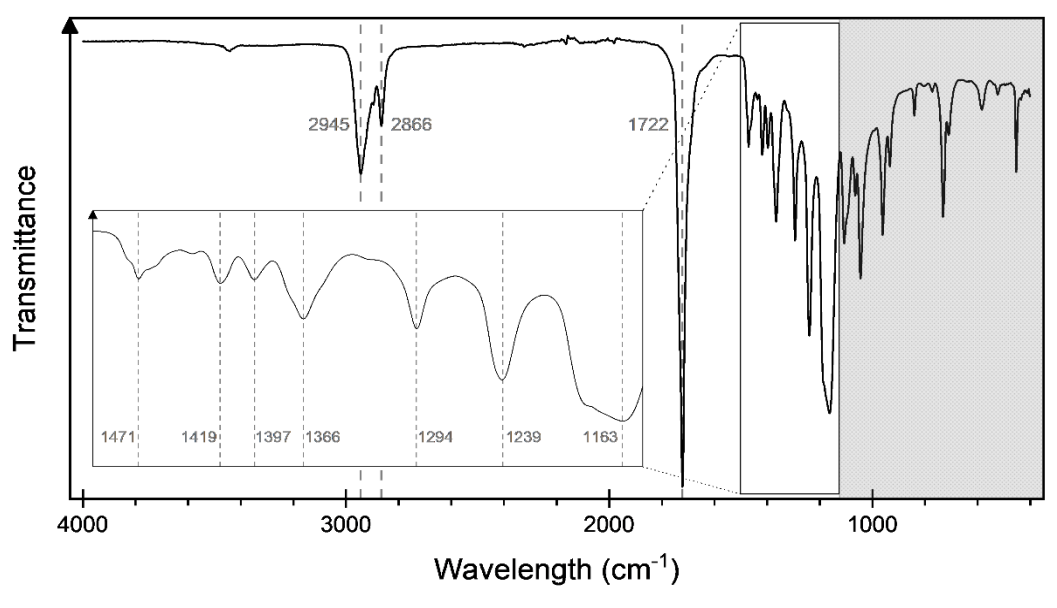


Figure 3.1 - PCL's Fourier Transform Infrared Spectroscopy analysis

Additionally, other peaks related to the polymer's molecular structure include those at 1419, 1397, and 1294 cm⁻¹, linked to C-C bond stretching, and peaks at 1471 cm⁻¹ and 1366 cm⁻¹, corresponding to CH₂ bending and CH₃ symmetric deformations, respectively.[41], [72] The peaks between 1000cm⁻¹ and 400 cm⁻¹ likely correspond to out-of-plane bending, wagging, and stretching of the polymer chain structure. [70]

Finally, the FTIR analysis of all composites, as illustrated in the graph in Figure 3.3, shows no new significant peaks. This indicates that no new chemical bonds were formed and the materials in the films did not undergo any compositional changes.

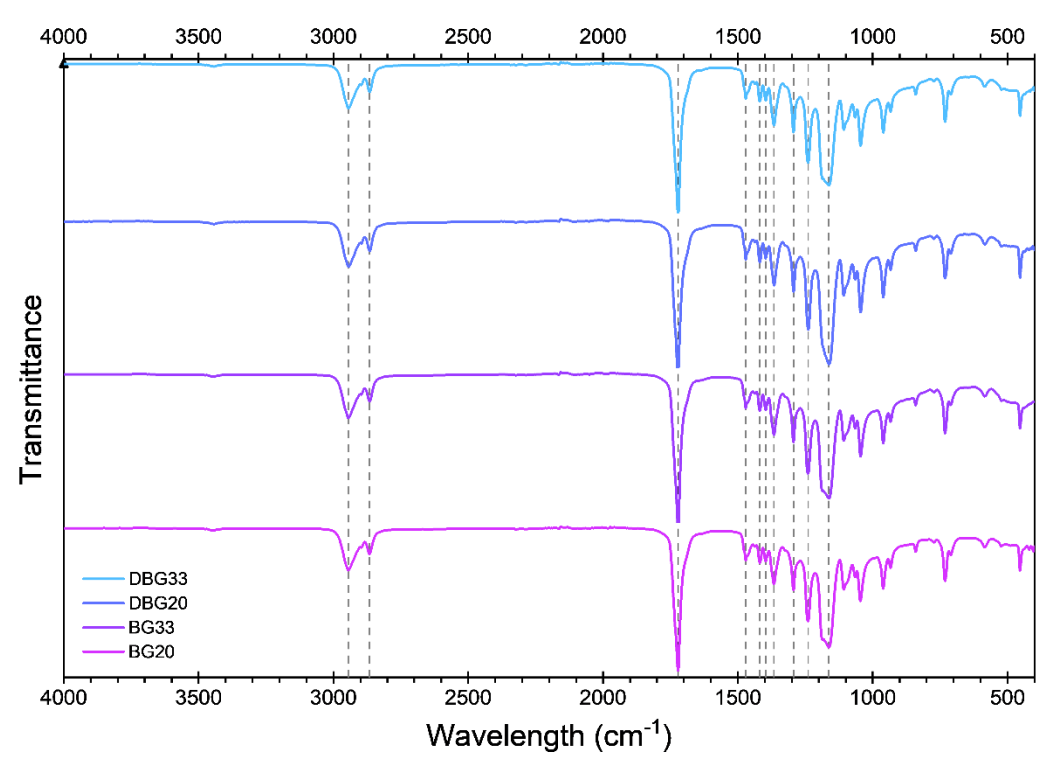


Figure 3.3 - PCL/BG composite's Fourier Transform Infrared Spectroscopy analysis

3.1.2 **SEM-EDS**

SEM images of BG and Mg-doped BG (Figure 3.4) showed heterogeneous particle sizes with uniform distribution. ImageJ analysis calculated average particle size from 903 BG and 1077 doped BG particles shown in Figure 3.5 and the parameters values presented in Table 3.1. EDS analysis (Figure 3.6) confirmed BG elements and Mg doping, with atomic percentages compared to theoretical values in Table 3.2.

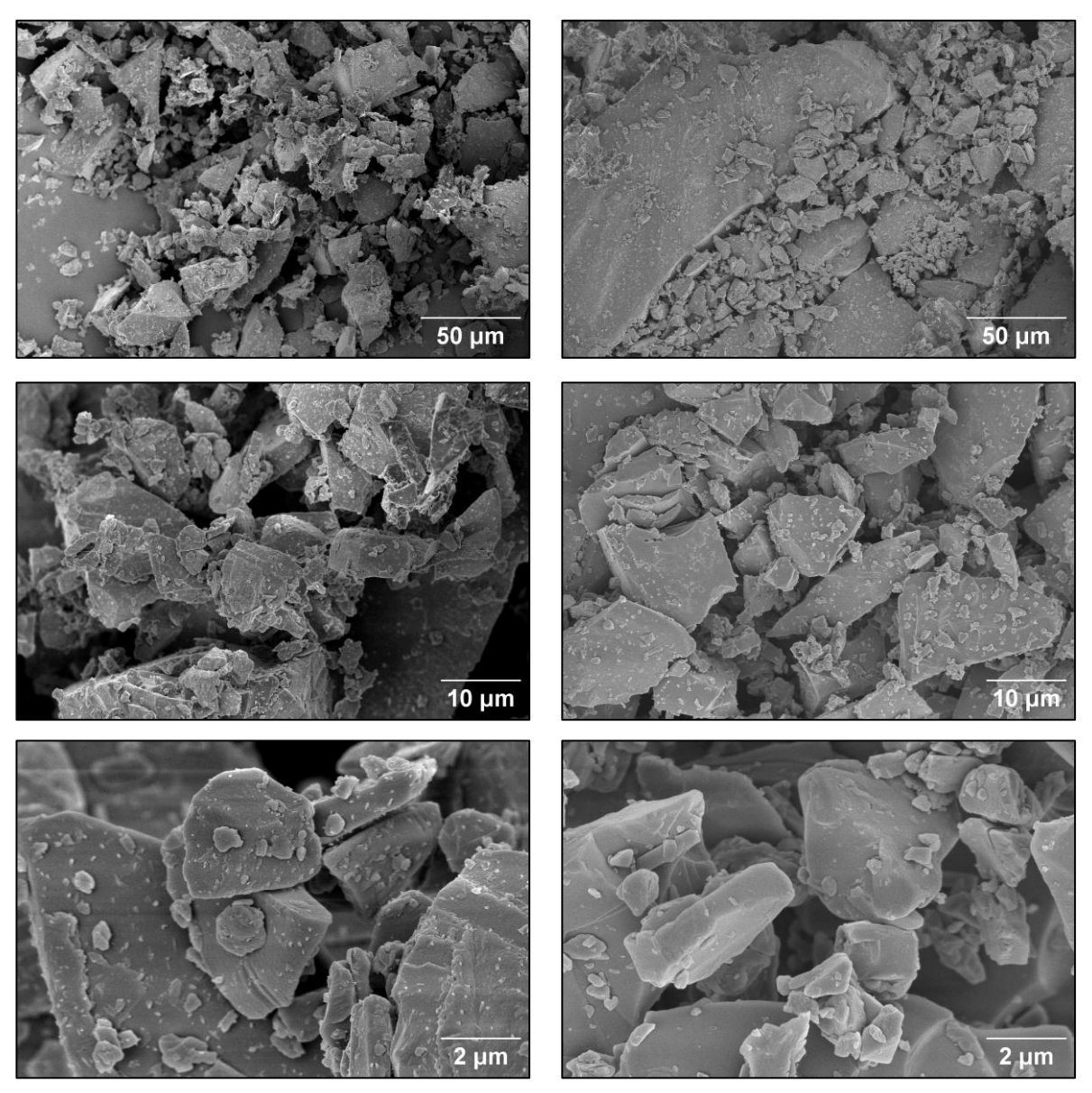
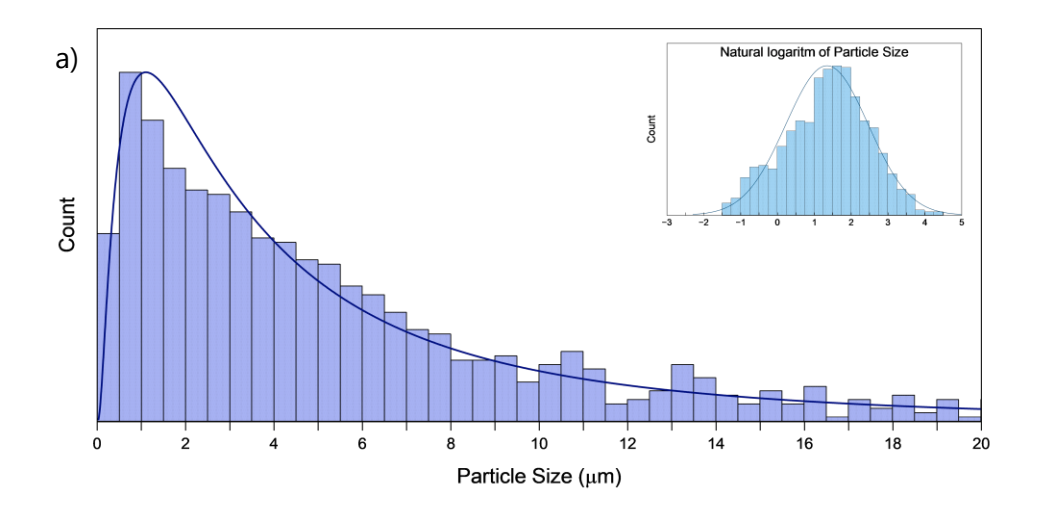


Figure 3.4 - SEM images of BG powder (on the left) and doped BG (on the right) with an ampliation of 500x, 2000x and 10000x (from top to bottom).

The particle size distribution of both BG and doped BG fits a lognormal distribution with the natural logarithm of particle size producing a normal distribution. The fitting of the distribution was made with the help of OriginPro[®] software, that used the lognormal probability distribution formula (1): [73], [74]

$$f(x) = \frac{1}{x\beta\sqrt{2\pi}} e^{\left(\frac{-(\ln(x)-\theta)}{2\beta}\right)^2}$$
 (1)



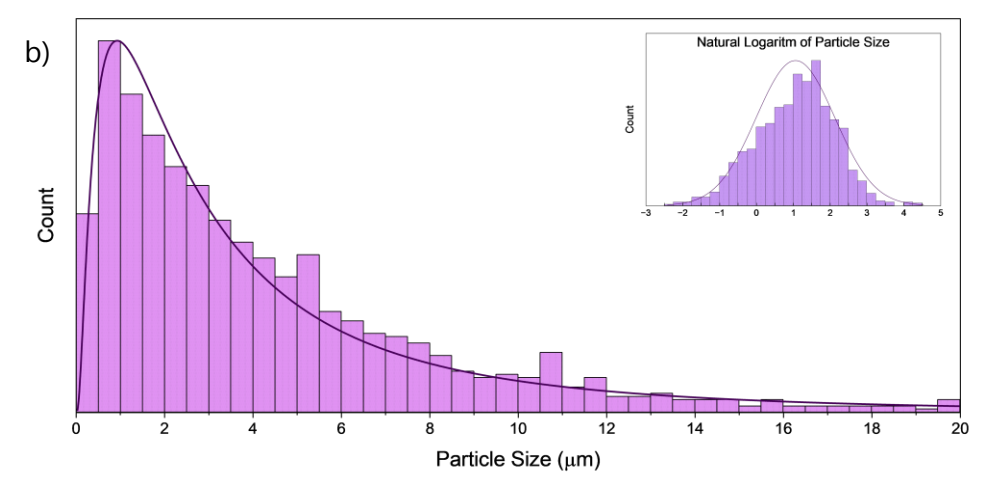


Figure 3.5 - Lognormal particle size distribution of BG (on top) and doped BG (on the bottom), with the respective normal distribution of the logarithm of the particle sizes.

Here, θ and β represent the mean and standard deviation of the normal distribution of the logarithm of the values, corresponding to the location and scale parameters of the log-normal distribution. The relationship between these values and the log-normal distribution parameters is illustrated by equations (2), (3), (4), and (5).[73], [74]

Median:
$$Med(X) = e^{\theta}$$
 (2)

Mean:
$$\mu = e^{\theta + \beta^2/2}$$
 (3)

Mode:
$$Mod(X) = e^{\theta + \beta^2}$$
 (4)

Variance:
$$\sigma^2 = (e^{\theta^2} - 1) \times e^{2\theta + \beta^2}$$
 (5)

Table 3.1 - Parameters of the lognormal particle size distributions.

						Standard
	Location ($ heta$)	Scale (β)	Med(X)	Mean (μ)	Mod(X)	Deviation (σ)
BG	1,353	1,120	3,868	7,242	1,103	11,465
Doped BG	1,067	1,068	2,908	5,146	0,929	7,512

The values also suggest that BG generally has larger and more variable particle sizes, whereas doped-BG shows a tighter distribution with smaller particles. The observed difference in particle size is unlikely due to Mg doping but rather to SEM imaging limitations, where larger particles are not fully captured while smaller ones are more easily detected, creating a bias toward smaller sizes, making the use of this technique a last resort.

All the elements present in BG, such as Si, P, Ca, Na, and O, were represented in EDS images, as well as Mg in the doped samples. The excessive oxygen content observed is likely the main cause of the discrepancies, as the relative atomic percentages are interconnected.

Despite this, the relative amounts and order of the elements in the composition chain were maintained, with the expected ratios remaining consistent. This suggests that while the absolute values might differ due to oxygen contamination, the general composition of both BG and Mg-doped BG remains structurally intact.

Table 3.2 - Theoretical and real values for Si, P, O, Ca, Na and Mg atomic percentages for SEM-EDS

		Si	Р	0	Ca	Na	Mg	Total
BG	Theoretical	16,27%	1,84%	55,22%	9,49%	17,18%	0%	100%
	Real	10,66%	1,06%	68,93%	6,21%	13,14%	0%	100%
BG-Mg	Theoretical	15,81%	1,78%	55,07%	9,22%	16,69%	1,43%	100%
	Real	10,24%	1,04%	69,82%	8,84%	9,05%	1%	100%

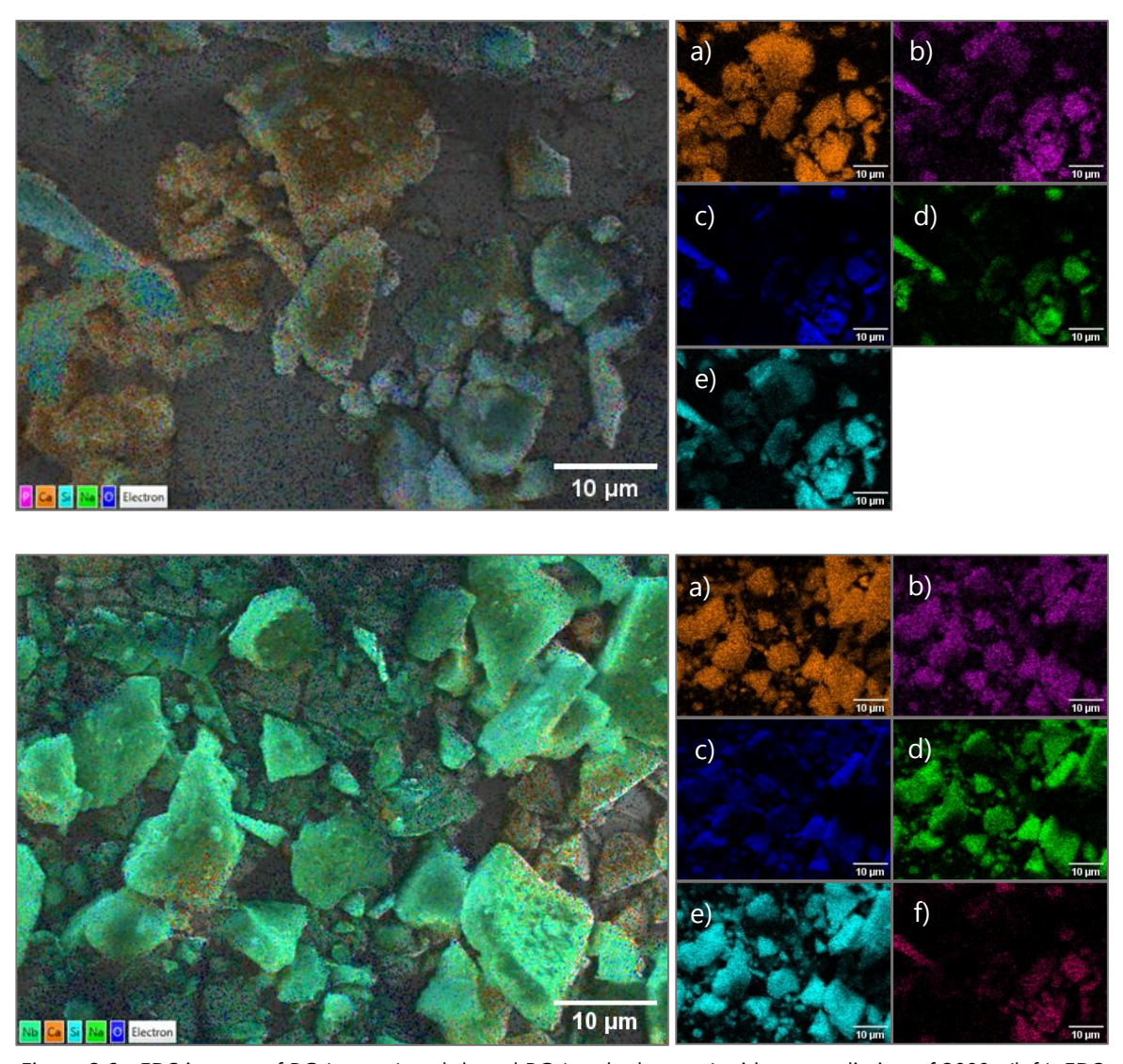


Figure 3.6 - EDS images of BG (on top) and doped BG (on the bottom) with an ampliation of 2000x (left). EDS images demonstrating Ca (a), P (b), O (c), Na (d), Si (e) and Mg (f) concentration (right)

3.1.3 Inductively Coupled Plasma (ICP) - Atomic Emission Spectroscopy

In Figure 3.7, the graphs display the concentrations of Ca, P, Na, Si, and Mg ions in the liquid. As the apatite layer forms, the composites absorb Ca and P ions from PBS to support growth. Doped BG consumes fewer ions than undoped BG, while lower BG content composites show higher ion absorption. Since the apatite layer mainly requires Ca and P, ions like Na, Si, and Mg are not retained.[43] Na and Si release is higher in undoped BG and composites with more BG, suggesting Mg-doping stabilizes the BG network and helps retain these ions. Mg release rises on day two, while Na and Si peak at 24 hours. Ca absorption increases after 24 hours, while P absorption decreases.[36]

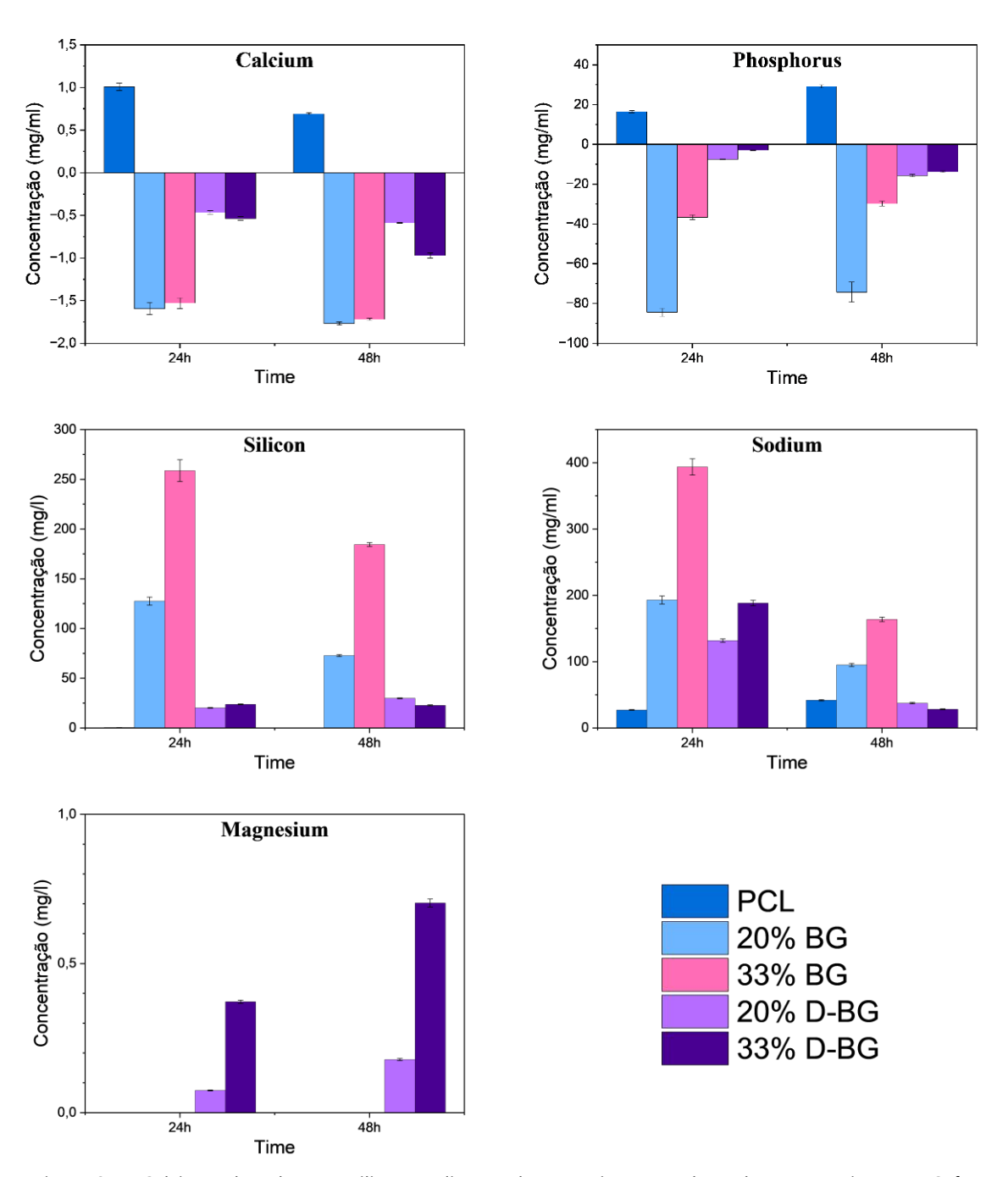
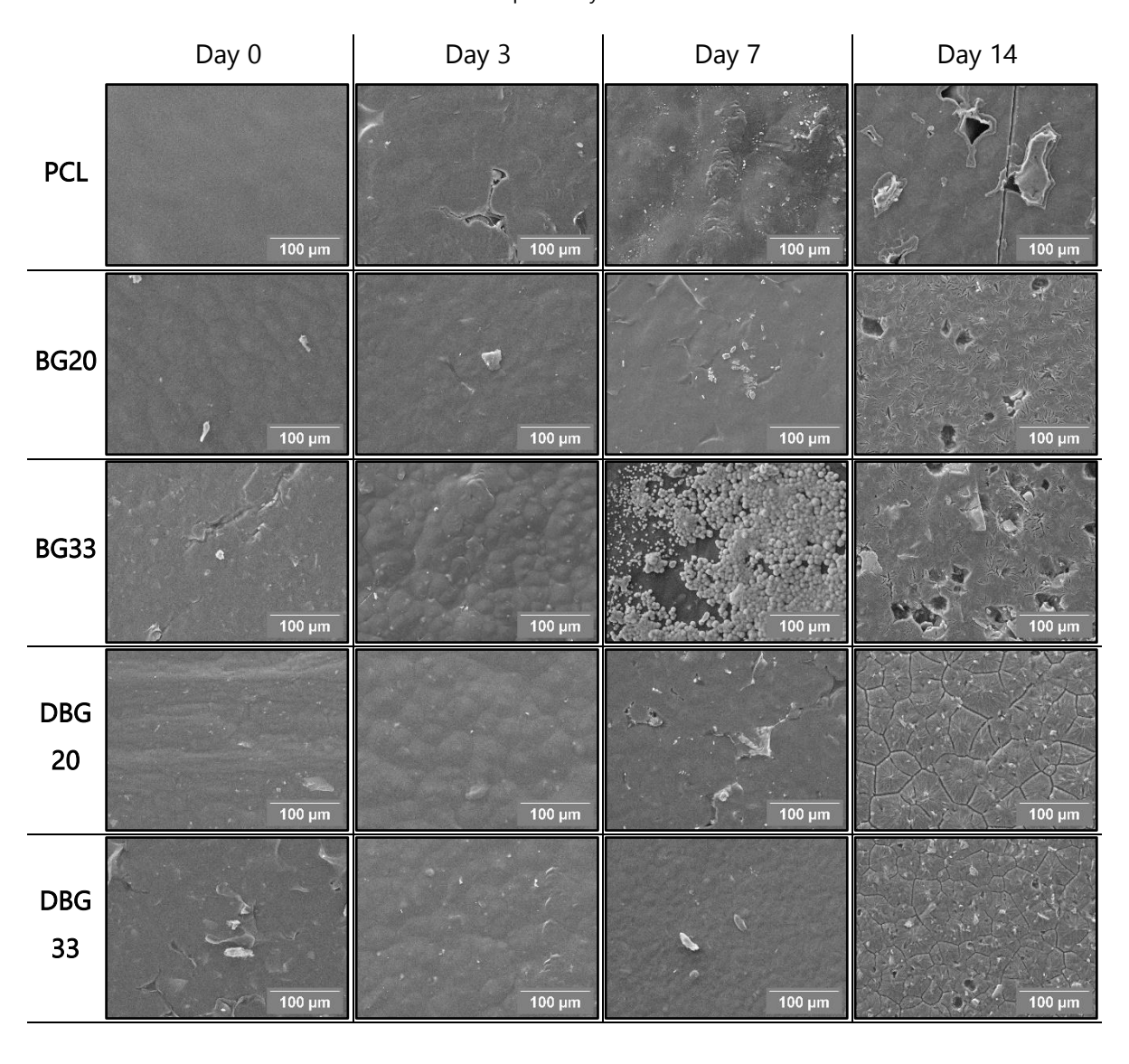


Figure 3.7 - Calcium, phosphorous, silicon, sodium and magnesium Ion released concentration to PBS, from ICP test results after 24 and 48 hours of submersion.

3.1.4 Bioactivity

The SEM images of the composite films immersed in SBF, presented in Table 3.3, tried to demonstrate the apatite layer formation in the samples containing BG. Visually, the composites with magnesium-doped BG exhibited more stable mineralization, as indicated by the more consistent layer formation.[8], [65]. However, the atomic percentages shown in Table 3.4 do not corroborate the visual results observed in the images.

Table 3.3 - SEM Images of PCL/BG composite's film surfaces after 0-, 3-, 7- and 14-periods of submersion in SBF, to assess apatite layer formation



PCL, composed of light elements, emits low-energy X-rays under electron bombardment, making detection challenging and prone to spectral overlap in EDS. Its poor conductivity and beam sensitivity can further cause artifacts and degradation. [75] - [77] These limitations make EDS highly unreliable for chemical characterization, as reflected by the atomic percentage values shown in Table 3.4, but it was used as a last resort since XRD, a more suitable technique, was unavailable.

Table 3.4 - Ca, Na, P, Si and Mg atomic percentage at film's surface, by EDS Imaging

		DAY 0	DAY3	DAY 7	DAY 14
PCL	Calcium	66,64%	10,55%	1,33%	70,68%
	Sodium	9,51%	8,65%	43,95%	0,38%
	Phosphorus	7,06%	80,18%	29,15%	0,76%
	Silicon	7,79%	0,46%	11,57%	27,81%
	Magnesium	9,00%	0,16%	13,99%	0,36%
BG20	Calcium	17,96%	49,68%	57,61%	69,89%
	Sodium	1,04%	6,70%	12,91%	3,41%
	Phosphorus	60,84%	35,73%	21,78%	25,17%
	Silicon	20,04%	7,82%	2,96%	0,02%
	Magnesium	0,11%	0,08%	4,73%	1,51%
BG33	Calcium	30,97%	39,02%	60,32%	55,65%
	Sodium	25,71%	8,01%	4,88%	6,78%
	Phosphorus	14,21%	36,60%	31,71%	31,24%
	Silicon	29,08%	14,91%	0,83%	4,54%
	Magnesium	0,03%	1,46%	2,26%	1,79%
DBG20	Calcium	41,78%	79,01%	58,63%	57,15%
	Sodium	17,23%	0,34%	4,35%	5,88%
	Phosphorus	17,28%	20,04%	26,93%	34,74%
	Silicon	23,65%	0,28%	10,07%	0,03%
	Magnesium	0,06%	0,32%	0,03%	2,20%
DBG33	Calcium	38,35%	24,44%	46,62%	62,73%
	Sodium	15,75%	9,69%	14,85%	3,04%
	Phosphorus	16,51%	34,98%	30,62%	33,60%
	Silicon	29,36%	25,07%	5,13%	0,12%
	Magnesium	0,03%	5,82%	2,78%	0,51%

3.1.5 Cytotoxicity

The graph in Figure 3.8 illustrates the viability of a cell culture in contact with different concentrations of non-passivated PCL, BG, and Mg-doped BG samples. The results show that PCL maintains high cell viability, confirming its biocompatibility Undoped BG significantly reduces cell viability, indicating strong cytotoxicity, especially at higher concentrations. This cytotoxic effect is noticeably reduced in the Mg-doped BG composites, which show improved viability, suggesting that magnesium doping mitigates the adverse effects observed with undoped BG. The slight variations in viability across the composites can likely be attributed to the high ion release, as previously noted by the ICP analysis, between the materials and the medium, which, in the case of undoped BG, increases pH and reduces cell viability, as shown by Ilyas, *et al.* (2022)[65], Amukarimi, *et al.* (2024)[37].

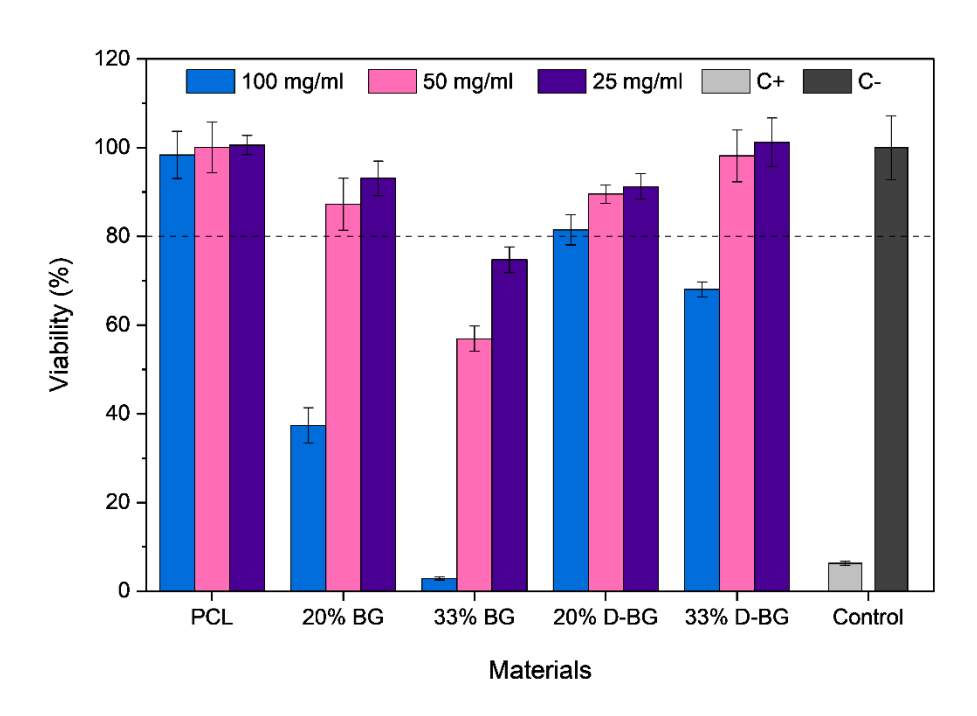


Figure 3.8 - Cytotoxicity assessment showing cell viability across different concentrations of PCL and PCL/BG composites.

3.1.6 Cell Adhesion and Proliferation

3.1.6.1 Cell population analysis

The results of the resazurin assays, displayed in Figure 3.9, align with the expected outcomes from cytotoxicity evaluation. Since this assay compares resazurin absorption in cells attached to the different samples with the control cells on the first day, variations in the data may arise from initial day results.

PCL continues to demonstrate excellent biocompatibility, as expected for an inert material. The composite with 33% BG shows significantly reduced cell viability, shrinking the cell population to a small fraction of the PCL-only samples. Lowering the BG concentration to 20% reduces cytotoxicity, promoting better cell adhesion and proliferation, though it still shows only marginal improvement over the 33% BG composite film.

Composites containing Mg-doped BG exhibit noticeably improved cell adhesion and proliferation compared to the undoped BG composites. The 33% Mg-doped BG composite performs similarly to the 20% undoped BG composite. Notably, the 20% Mg-doped BG composite shows the best overall results, displaying enhanced cell proliferation, even surpassing that observed in the PCL samples, as shown in Table 3.5.

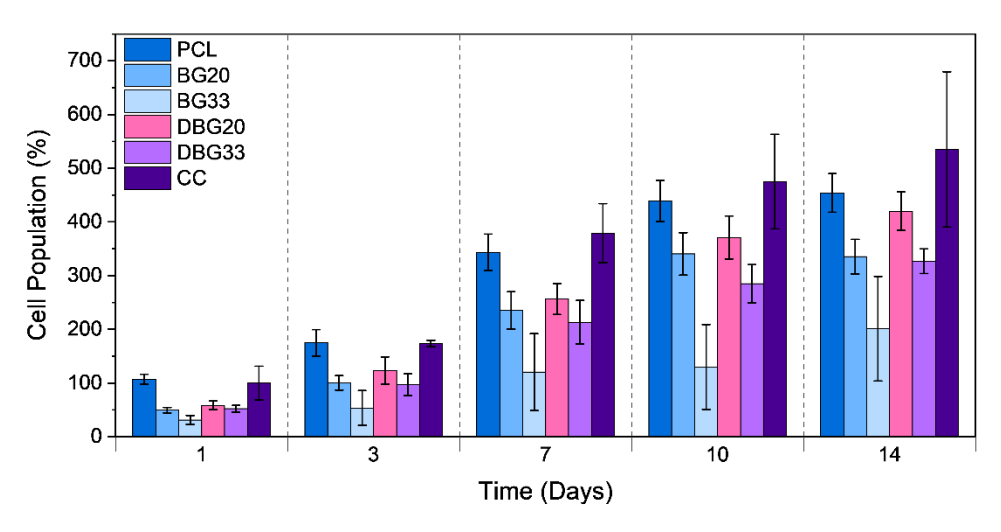


Figure 3.9 - Cell adhesion and proliferation of SaOs-2 on PCL and PCL/BG composites films over various time periods (1-, 3-, 7-, 10- and 14-days) measured using resazurin assays.

Table 3.5 - Proliferation of SaOs-2 cells on each material, expressed as final day/initial day percentage.

Materials	Proliferation
PCL	423%
BG20	388%
BG33	679%
DBG20	627%
DBG33	641%

3.1.6.2 ALP

The ALP production data in Figure 3.10, with large error bars likely result from issues in preparing the tris-hydrochloric acid buffer, where excessive hydrochloric acid was required to balance an initially basic solution, complicating pH calibration and rendering the results scientifically unreliable.

Despite this, the data in Figure 3.10 clearly indicates that samples with higher cell adhesion did not exhibit proportional ALP activity. This could be explained by the fact that larger cell populations have to share limited space in the substrate, potentially lowering their activity and consequently ALP production. For the samples containing Bioglass®, magnesium doping noticeably enhances cell activity. Early on, this effect is more prominent in less concentrated films, while in later stages, as the cell populations grow, the improvement becomes more apparent in higher concentration samples.

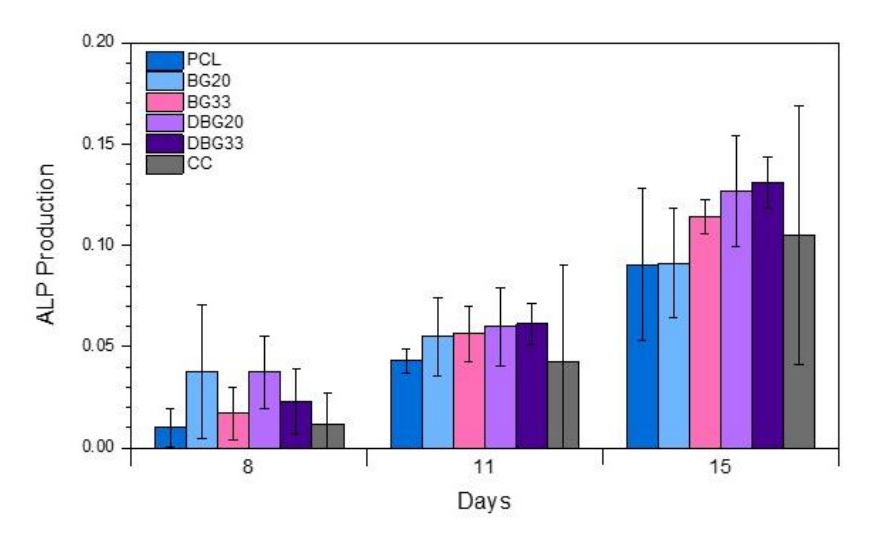


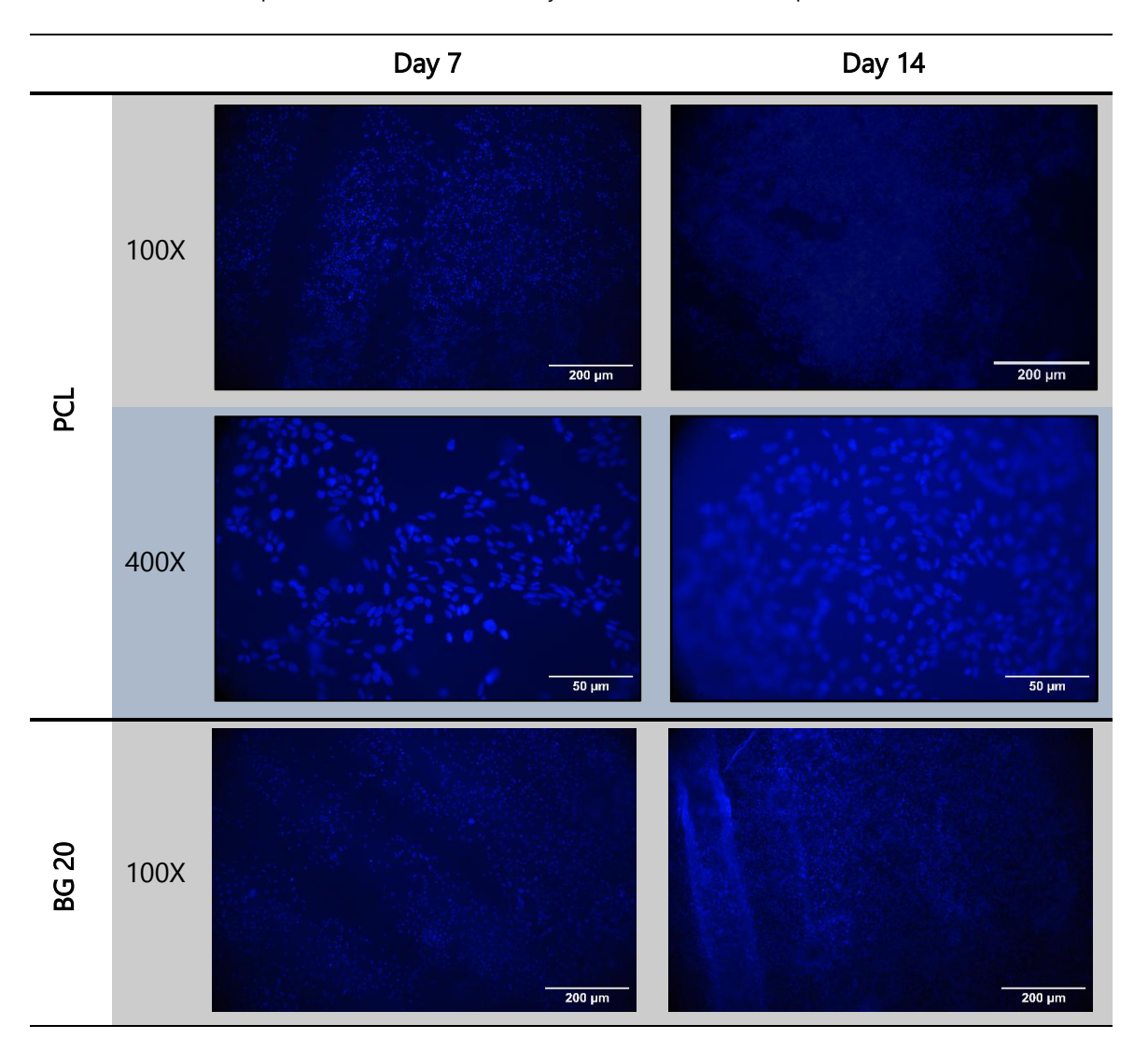
Figure 3.10- Cell activity of SaOs-2 on PCL and PCL/BG composites films over various time periods (8-, 11- and 15-days) measured by ALP production.

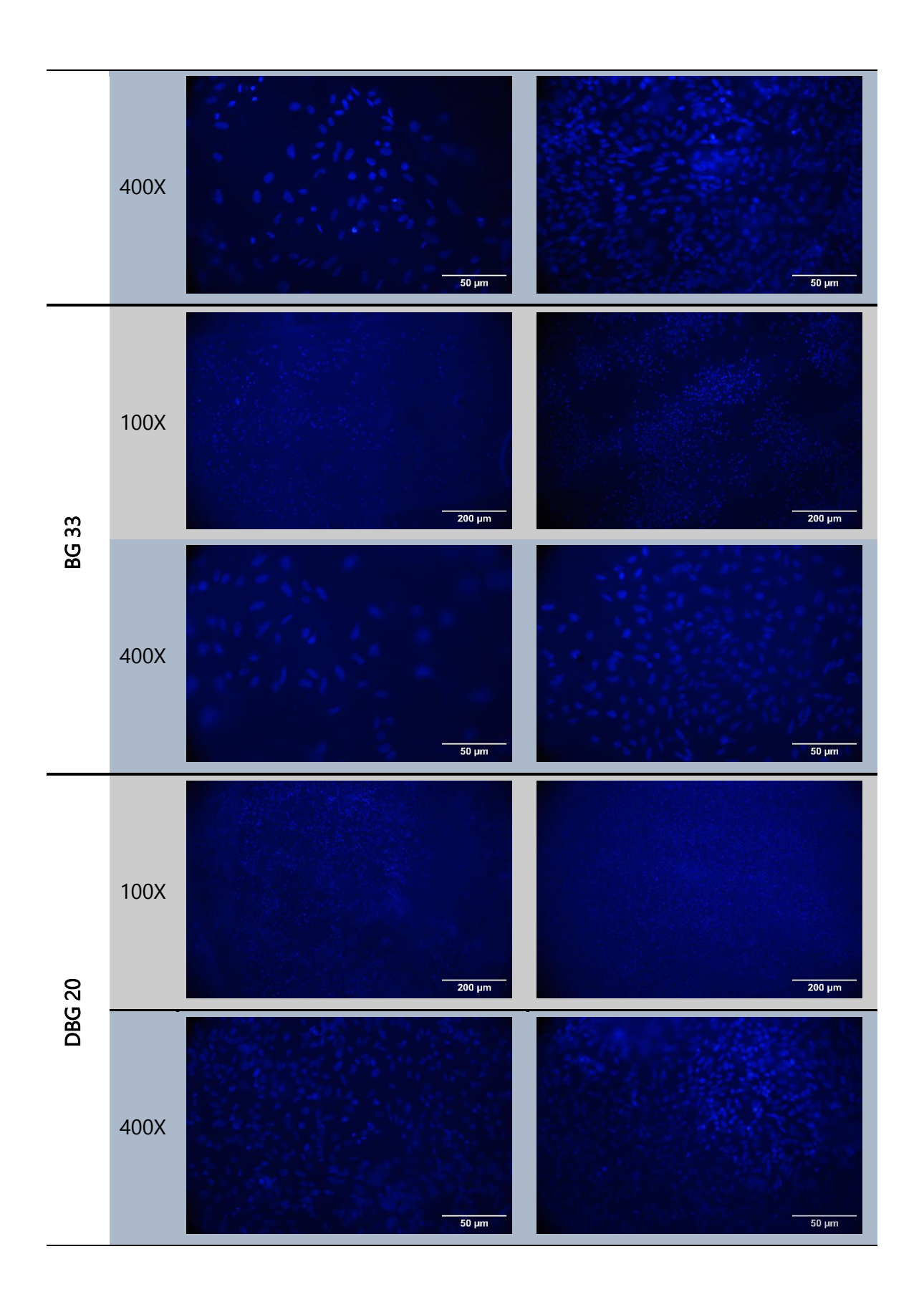
The samples with more adherent cells show lower ALP activity, and Mg-doped samples show increased ALP production over time, particularly in the more concentrated composites. There have been multiple reports of these results by Gavinho, *et al.* (2023)[8], Sharifianjazi, *et al.* (2020)[36], Sergi, *et al.* (2020)[41] and Moghanian, *et al.* (2018)[44]

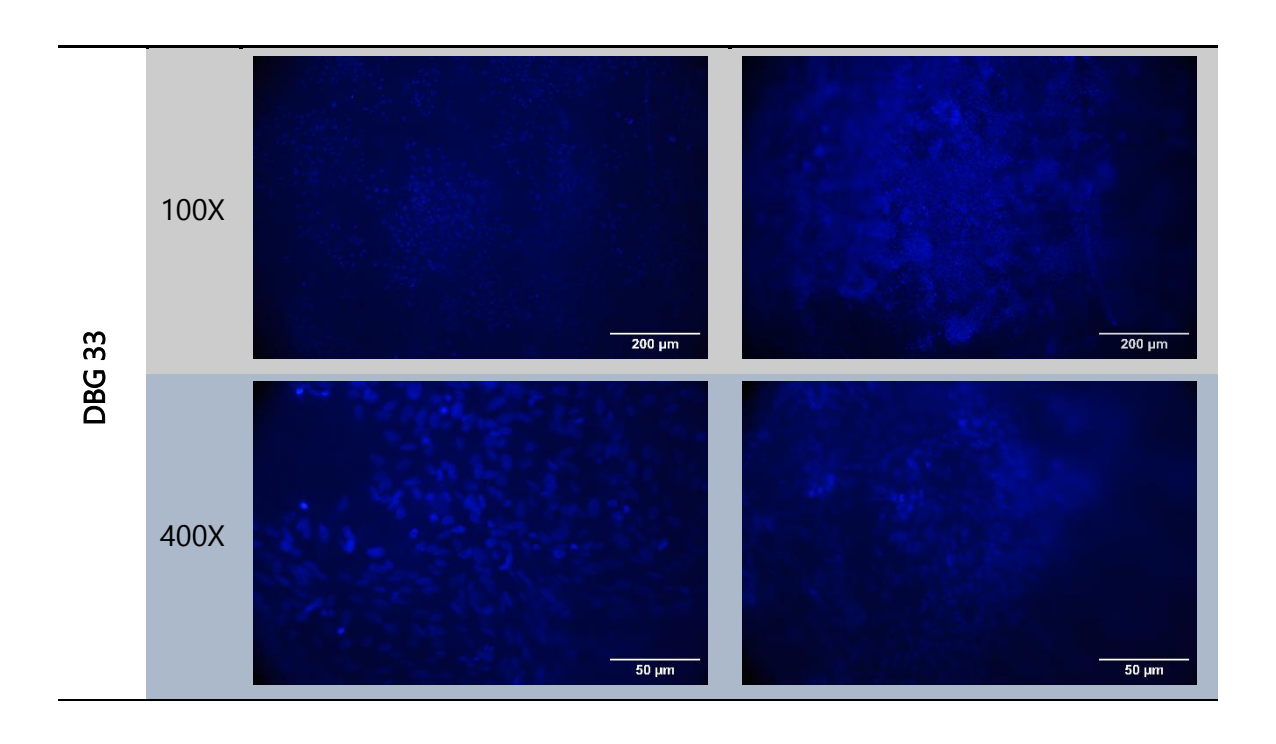
3.1.6.3 Fluorescence

A miscalculation in the phalloidin concentration resulted in the images not displaying any fluorescence and the cytoskeleton could not be observed. However, the DAPI staining images in Table 3.6 clearly reveals numerous cell nuclei, particularly after 14 days of incubation. The images align with the results from the resazurin assays, showing higher cell concentrations in the PCL and doped BG samples compared to the undoped BG samples

Table 3.6 - DAPI fluorescence staining images showing the nuclei of cells adhered to the surface of PCL and PCL/BG composite films after 7 and 14 days of incubation, with ampliation of 100x and 400x.







3.2 Discussion

The FTIR analysis from Figures 3.1, 3.2 and 3.3 showed characteristic peaks for both PCL and BG, confirming the presence of key functional groups. Additionally, no new peaks were observed in the composite, suggesting that the PCL and BG were physically mixed without chemical bonding, as expected. Despite the physical combination, impurities like C-H and CO₃²⁻ groups were detected, likely introduced during sample cleaning and through atmospheric contamination, as by the atomic percentage analysis of BG and doped-BG powder. [67], [69], [71] The particle size distribution of BG and doped BG showed a tendency toward smaller particles because larger ones couldn't fit entirely in the SEM images. This limits the accuracy of the measurements, so using more advanced techniques such as Static Light Scattering (SLS) and Dynamic Light Scattering (DLS) is recommended.[73], [74] Magnesium alters BG's mechanical properties by acting as a network modifier, disrupting Si–O–Si bonds and introducing non-bridging oxygens. This structural change reduces brittleness and increases hardness, stiffness, and fracture resistance. Proper testing using methods like Atomic Force Microscopy (AFM) or Micro-Hardness measurements is crucial to confirm these effects, as they influence the material's durability and suitability for bone regeneration applications.[8], [36]

The EDS analysis of BG and doped-BG powders revealed deviations in the atomic percentages of silicon, calcium, phosphorus, sodium, and magnesium compared to theoretical values, likely due to excess oxygen contamination or incorporation into the BG's amorphous structure.

Despite these discrepancies, the overall composition order remained consistent, confirming the presence of Mg in the doped BG samples. However, accurately detecting these elements in composite films submerged in SBF proved challenging. The analysis of apatite formation using EDS and SEM images was inconclusive, largely due to the limitations of the tabletop SEM used. Its restricted sensitivity, combined with the PCL coating covering the BG particles, hindered the accurate EDS assessment for apatite layer formation on the film surfaces. Utilizing a XRD technique would improve the ability to analyse the scaffold surfaces and apatite development, allowing for a more precise evaluation of bioactivity. [75] - [77]

The ICP analysis results confirm that BG releases a high concentration of sodium and silicon, while absorbing significant amounts of calcium and phosphorus from the surrounding medium. This ion absorption is linked to faster apatite layer formation, indicating less stable bioactivity. The high ion release rate also explains the notable pH increase, which contributes to the observed cytotoxicity. However, doping BG with magnesium reduces both ion release and absorption, mitigating cytotoxicity and promoting more stable apatite formation. These results were shown by Jo, *et al.* (2024)[43] and Moghanian, *et al.* (2018)[44]

In terms of cytotoxicity, the resazurin assay and ALP tests showed that undoped BG exhibits some level of toxicity, which negatively affects osteoblast adhesion and proliferation. This cytotoxicity can be attributed to the significant ion release from the BG into the medium, as indicated by the ICP results. The high concentration of released ions alters the pH of the medium, making it unfavourable for cell growth. In contrast, doping BG with magnesium significantly reduces the ion release, as evidenced by the lower concentrations of ions detected in the medium. This reduction in ion release likely explains the decreased cytotoxicity observed in the doped-BG samples.[37], [48], [65], [78]

Despite the limitations in elemental analysis, the resazurin and ALP assays consistently demonstrated that doped BG promotes better cell adhesion and proliferation compared to undoped BG, as shown by Gavinho, *et al.* (2023)[8] and Sharifianjazi, *et al* (2020)[36]. The higher cell viability observed in PCL and doped-BG samples suggests that magnesium doping improves the material's biocompatibility by reducing the toxic ion concentration in the medium. This supports the notion that doping BG can modulate its cytotoxic effects, making it a more suitable material for tissue engineering.

CONCLUSION AND FUTURE PERSPECTIVES

The results of this study highlight key findings in the potential of PCL/BG composite films as surface coatings. Magnesium-doped BG composites were found to exhibit improved bioactivity, as demonstrated by their ability to promote more stable apatite formation over time compared to undoped BG.

Cell adhesion and proliferation assays, specifically using human osteosarcoma cells (SaOS-2), further support the superior performance of Mg-doped composites. Not only do these composites have better cell adhesion, but they also promote higher cell viability and proliferation rates. The study results correlated undoped BG's cytotoxicity to its high ion release concentration, which altered the pH of the surrounding medium, negatively impacting cell growth. In contrast, Mg doping mitigates this by stabilizing ion release and reducing the associated cytotoxicity.

Thus, Mg-doped BG emerges as a more biocompatible option for bone tissue engineering, suggesting its potential for future applications in bone regeneration.

Looking forward, several improvements should be explored to optimize the performance of PCL/BG composite scaffolds for clinical applications. One key area is the printability of PCL/BG composites. Future research should focus on developing filaments that incorporate these composites, ensuring they maintain both mechanical integrity and biocompatibility during the 3D printing process. Evaluating the mechanical, biological, and structural properties of these printed scaffolds is essential to ensure they can meet the physical requirements of bone tissue regeneration without compromising it.

Porosity is another critical factor for scaffold design, as it directly impacts cell infiltration, nutrient diffusion, and overall tissue growth. Future studies should try and optimize the porosity of 3D-printed scaffolds, aiming to create structures that mimic the porous architecture of natural bone.

Additionally, alternative 3D printing techniques should be explored to determine the most effective method for fabricating PCL/BG composite scaffolds.

Finally, designing 3D-printed scaffolds that are moulded for specific human bone shapes will be a crucial step in personalizing treatments for bone defects. By combining advanced imaging techniques with addictive manufacturing, patient-specific scaffolds can be developed to better fit the defect site, enhancing the integration of the scaffold with the surrounding tissue.

In conclusion, while PCL/BG composite films show significant promise for enhancing the bioactivity of PLA-based scaffolds, there is a need for further investigation into scaffolding 3D printability, mechanical and structural properties, and their clinical applicability. By addressing these challenges, the potential of 3D printing and PCL/BG composite scaffolds in bone regeneration can be fully realized.

BIBLIOGRAPHY

- [1] N. Su *et al.*, "Bone function, dysfunction and its role in diseases including critical illness," 2019, *Ivyspring International Publisher*. doi: 10.7150/ijbs.27063.
- [2] R. Florencio-Silva *et al.*, "Biology of Bone Tissue: Structure, Function, and Factors That Influence Bone Cells," 2015, *Hindawi Publishing Corporation*. doi: 10.1155/2015/421746.
- [3] J. Black and B. Tadros, "Bone structure: from cortical to calcium," *Orthop Trauma*, vol. 34, no. 3, pp. 113–119, Jun. 2020, doi: 10.1016/j.mporth.2020.03.002.
- [4] M. Ponzetti and N. Rucci, "Osteoblast differentiation and signaling: Established concepts and emerging topics," Jul. 01, 2021, *MDPI*. doi: 10.3390/ijms22136651.
- [5] G. Zhu *et al.*, "Bone physiological microenvironment and healing mechanism: Basis for future bone-tissue engineering scaffolds," Nov. 01, 2021, *KeAi Communications Co.* doi: 10.1016/j.bioactmat.2021.03.043.
- [6] K. Arvidson *et al.*, "Bone regeneration and stem cells," 2011, *Blackwell Publishing Inc.* doi: 10.1111/j.1582-4934.2010.01224.x.
- [7] G. Hutchings *et al.*, "Bone regeneration, reconstruction and use of osteogenic cells; from basic knowledge, animal models to clinical trials," Jan. 01, 2020, *MDPI*. doi: 10.3390/jcm9010139.
- [8] S. Gavinho *et al.*, "Bioactive Glasses Containing Strontium or Magnesium Ions to Enhance the Biological Response in Bone Regeneration," *Nanomaterials*, vol. 13, no. 19, Oct. 2023, doi: 10.3390/nano13192717.
- [9] L. Theyse *et al.*, "Growth hormone stimulates bone healing in a critical-sized bone defect model," *Clin Orthop Relat Res*, vol. 446, pp. 259–267, 2006, doi: 10.1097/01.blo.0000203490.21206.7f.
- [10] E. Jones and X. Yang, "Mesenchymal stem cells and bone regeneration: Current status," *Injury*, vol. 42, no. 6, pp. 562–568, 2011, doi: 10.1016/j.injury.2011.03.030.

- [11] Y. Yan *et al.*, "Vascularized 3D printed scaffolds for promoting bone regeneration," *Biomaterials*, vol. 190–191, pp. 97–110, Jan. 2019, doi: 10.1016/j.biomaterials.2018.10.033.
- [12] R. Dimitriou *et al.*, "Bone regeneration: Current concepts and future directions," May 31, 2011. doi: 10.1186/1741-7015-9-66.
- [13] E. Rezvani Ghomi *et al.*, "Collagen-based biomaterials for biomedical applications," Dec. 01, 2021, *John Wiley and Sons Inc.* doi: 10.1002/jbm.b.34881.
- [14] S. Winn *et al.*, "Gene therapy approaches for modulating bone regeneration," 2000. [Online]. Available: www.elsevier.com/locate/drugdeliv
- [15] M. Bez, G. Pelled, and D. Gazit, "BMP gene delivery for skeletal tissue regeneration," Aug. 01, 2020, *Elsevier Inc.* doi: 10.1016/j.bone.2020.115449.
- [16] V. Bunpetch *et al.*, "Strategies for MSC expansion and MSC-based microtissue for bone regeneration," *Biomaterials*, vol. 196, pp. 67–79, Mar. 2019, doi: 10.1016/j.biomaterials.2017.11.023.
- [17] A. Oryan, S. Alidadi, and A. Moshiri, "Platelet-rich plasma for bone healing and regeneration," *Expert Opin Biol Ther*, vol. 16, no. 2, pp. 213–232, Feb. 2016, doi: 10.1517/14712598.2016.1118458.
- [18] K. Alvarez and H. Nakajima, "Metallic scaffolds for bone regeneration," *Materials*, vol. 2, no. 3, pp. 790–832, 2009, doi: 10.3390/ma2030790.
- [19] P. Wang *et al.*, "Biodegradable Implants for Internal Fixation of Fractures and Accelerated Bone Regeneration," Aug. 08, 2023, *American Chemical Society*. doi: 10.1021/acsomega.3c02727.
- [20] R. Verboket *et al.*, "Autologous cell-based therapy for treatment of large bone defects: from bench to bedside," Oct. 01, 2018, *Springer Berlin Heidelberg*. doi: 10.1007/s00068-018-0906-y.
- [21] M. Collins *et al.*, "Scaffold Fabrication Technologies and Structure/Function Properties in Bone Tissue Engineering," May 01, 2021, *John Wiley and Sons Inc.* doi: 10.1002/adfm.202010609.
- [22] B. Safari, S. Davaran, and A. Aghanejad, "Osteogenic potential of the growth factors and bioactive molecules in bone regeneration," Apr. 01, 2021, *Elsevier B.V.* doi: 10.1016/j.ijbiomac.2021.02.052.
- [23] A. Plachokova *et al.*, "Effect of platelet-rich plasma on bone regeneration in dentistry: A systematic review," *Clin Oral Implants Res*, vol. 19, no. 6, pp. 539–545, Jun. 2008, doi: 10.1111/j.1600-0501.2008.01525.x.

- [24] T. Turvey *et al.*, "The use of self-reinforced biodegradable bone plates and screws in orthognathic surgery," *Journal of Oral and Maxillofacial Surgery*, vol. 60, no. 1, pp. 59–65, 2002, doi: 10.1053/joms.2002.28274.
- [25] J. Li *et al.*, "Materials evolution of bone plates for internal fixation of bone fractures: A review," Jan. 01, 2020, *Chinese Society of Metals*. doi: 10.1016/j.jmst.2019.07.024.
- [26] M. Ridzwan *et al.*, "Problem of stress shielding and improvement to the hip implant designs: A review," Apr. 01, 2007, *Asian Network for Scientific Information*. doi: 10.3923/jms.2007.460.467.
- [27] M. Dobrzyńska-Mizera *et al.*, "Engineering of Bioresorbable Polymers for Tissue Engineering and Drug Delivery Applications," 2024, *John Wiley and Sons Inc.* doi: 10.1002/adhm.202401674.
- [28] G. El Fawal *et al.*, "Fabrication of scaffold based on gelatin and polycaprolactone (PCL) for wound dressing application," *J Drug Deliv Sci Technol*, vol. 63, Jun. 2021, doi: 10.1016/j.jddst.2021.102501.
- [29] A. Singh, K. Pramanik, and A. Biswas, "MgO enables enhanced bioactivity and antimicrobial activity of nano bioglass for bone tissue engineering application," *Materials Technology*, vol. 34, no. 13, pp. 818–826, Nov. 2019, doi: 10.1080/10667857.2019.1638636.
- [30] N. Siddiqui *et al.*, "PCL-Based Composite Scaffold Matrices for Tissue Engineering Applications," Jul. 01, 2018, *Humana Press Inc.* doi: 10.1007/s12033-018-0084-5.
- [31] T. De Witte *et al.*, "Bone tissue engineering via growth factor delivery: From scaffolds to complex matrices," *Regen Biomater*, vol. 5, no. 4, pp. 197–211, Aug. 2018, doi: 10.1093/rb/rby013.
- [32] V. Mouriño and A. Boccaccini, "Bone tissue engineering therapeutics: Controlled drug delivery in three-dimensional scaffolds," Feb. 06, 2010, *Royal Society.* doi: 10.1098/rsif.2009.0379.
- [33] E. Piatti *et al.*, "Poly(ε-caprolactone)/bioactive glass composite electrospun fibers for tissue engineering applications," *J Biomed Mater Res A*, vol. 111, no. 11, pp. 1692–1709, Nov. 2023, doi: 10.1002/jbm.a.37578.
- [34] K. Kolan *et al.*, "Solvent Based 3D Printing of Biopolymer/Bioactive Glass Composite and Hydrogel for Tissue Engineering Applications," in *Procedia CIRP*, Elsevier B.V., 2017, pp. 38–43. doi: 10.1016/j.procir.2017.04.022.
- [35] N. Gómez-Cerezo *et al.*, "Effects of a mesoporous bioactive glass on osteoblasts, osteoclasts and macrophages," *J Colloid Interface Sci*, vol. 528, pp. 309–320, Oct. 2018, doi: 10.1016/j.jcis.2018.05.099.

- [36] F. Sharifianjazi *et al.*, "Effects of Sr and Mg dopants on biological and mechanical properties of SiO2–CaO–P2O5 bioactive glass," *Ceram Int*, vol. 46, no. 14, pp. 22674–22682, Oct. 2020, doi: 10.1016/j.ceramint.2020.06.030.
- [37] S. Amukarimi, M. Zadshakoyan, and I. Mobasherpour, "Fabrication and characterization of strontium- and copper-doped bioactive glasses modified biodegradable MgO-PCL coated magnesium biomaterials," *Appl Phys A Mater Sci Process*, vol. 130, no. 10, Oct. 2024, doi: 10.1007/s00339-024-07878-w.
- [38] M. Edén, "Structure and formation of amorphous calcium phosphate and its role as surface layer of nanocrystalline apatite: Implications for bone mineralization," *Materialia* (Oxf), vol. 17, Jun. 2021, doi: 10.1016/j.mtla.2021.101107.
- [39] D. Morais *et al.*, "Surface functionalization of polypropylene (PP) by chitosan immobilization to enhance human fibroblasts viability," *Polym Test*, vol. 86, Jun. 2020, doi: 10.1016/j.polymertesting.2020.106507.
- [40] D. Goel and D. Santhiya, "Tunable structural, optical and bioactive properties of magnesium and bismuth co-doping on bioactive glass nanoparticles for biomedical applications," *J Mater Res*, 2024, doi: 10.1557/s43578-024-01433-2.
- [41] R. Sergi *et al.*, "Incorporation of bioactive glasses containing Mg, Sr, and Zn in electrospun PCL fibers by using benign solvents," *Applied Sciences (Switzerland)*, vol. 10, no. 16, Aug. 2020, doi: 10.3390/app10165530.
- [42] N. Ibrahim, H. Mohamad, and S. Mohd Noor, "Characterization on melt-derived bioactive glass powder from SiO2-CaO-Na2O-P2O5 system," *J Non Cryst Solids*, vol. 462, pp. 23–31, Apr. 2017, doi: 10.1016/j.jnoncrysol.2017.01.040.
- [43] H. Jo *et al.*, "Bioactive Ions-Loaded Bioinks Primed for 3D Printing of Artificial Tissues," Sep. 01, 2024, *Springer Nature*. doi: 10.1007/s44174-023-00151-3.
- [44] A. Moghanian *et al.*, "The effect of magnesium content on in vitro bioactivity, biological behavior and antibacterial activity of sol–gel derived 58S bioactive glass," *Ceram Int*, vol. 44, no. 8, pp. 9422–9432, Jun. 2018, doi: 10.1016/j.ceramint.2018.02.159.
- [45] X. Wang *et al.*, "Synthesis and characterization of hierarchically macroporous and mesoporous CaO-MO-SiO2-P2O5 (M = Mg, Zn, Sr) bioactive glass scaffolds," *Acta Biomater*, vol. 7, no. 10, pp. 3638–3644, 2011, doi: 10.1016/j.actbio.2011.06.029.
- [46] M. Ebrahimi, S. Manafi, and F. Sharifianjazi, "The effect of Ag2O and MgO dopants on the bioactivity, biocompatibility, and antibacterial properties of 58S bioactive glass synthesized by the sol-gel method," *J Non Cryst Solids*, vol. 606, Apr. 2023, doi: 10.1016/j.jnoncrysol.2023.122189.

- [47] S. Kargozar *et al.*, "Osteogenic Potential of Magnesium (Mg)-Doped Multicomponent Bioactive Glass: In Vitro and In Vivo Animal Studies," *Materials*, vol. 15, no. 1, Jan. 2022, doi: 10.3390/ma15010318.
- [48] D. Zhang *et al.*, "Antibacterial effects and dissolution behavior of six bioactive glasses," *J Biomed Mater Res A*, vol. 93, no. 2, pp. 475–483, May 2010, doi: 10.1002/jbm.a.32564.
- [49] I. Allan, H. Newman, and M. Wilson, "Antibacterial activity of particulate Bioglass against supra-and subgingival bacteria," 2001.
- [50] © 2023 lota Sigma Group Plastic manufacturers UK, "Rapid Prototyping Selective Laser Sintering," http://www.iotasigma.co.uk/sls.html. Accessed: Jan. 11, 2024. [Online]. Available: http://www.iotasigma.co.uk/sls.html
- [51] Kudo 3D, "SLA 3D Printing: Difference in Laser and DLP Light Pattern Generation." Accessed: Jan. 10, 2024. [Online]. Available: https://www.kudo3d.com/sla-3d-printing-difference-in-laser-and-dlp-light-generation/
- [52] I. Theodorakos, F. Zacharatos, R. Geremia, D. Karnakis, and I. Zergioti, "Selective laser sintering of Ag nanoparticles ink for applications in flexible electronics," in *Applied Surface Science*, Elsevier B.V., May 2015, pp. 157–162. doi: 10.1016/j.apsusc.2014.10.120.
- [53] R. Chen, W. Duan, G. Wang, B. Liu, Y. Zhao, and S. Li, "Preparation of broadband transparent Si3N4-SiO2 ceramics by digital light processing (DLP) 3D printing technology," *J Eur Ceram Soc*, vol. 41, no. 11, pp. 5495–5504, Sep. 2021, doi: 10.1016/j.jeurceramsoc.2021.04.045.
- [54] H. Quan, T. Zhang, H. Xu, S. Luo, J. Nie, and X. Zhu, "Photo-curing 3D printing technique and its challenges," Mar. 01, 2020, *KeAi Communications Co.* doi: 10.1016/j.bioact-mat.2019.12.003.
- [55] A. Awad, F. Fina, A. Goyanes, S. Gaisford, and A. W. Basit, "3D printing: Principles and pharmaceutical applications of selective laser sintering," *Int J Pharm*, vol. 586, Aug. 2020, doi: 10.1016/j.ijpharm.2020.119594.
- [56] M. E. Imanian and F. R. Biglari, "Modeling and prediction of surface roughness and dimensional accuracy in SLS 3D printing of PVA/CB composite using the central composite design," *J Manuf Process*, vol. 75, pp. 154–169, Mar. 2022, doi: 10.1016/j.jma-pro.2021.12.065.
- [57] M. Mukhtarkhanov, A. Perveen, and D. Talamona, "Application of stereolithography based 3D printing technology in investment casting," Oct. 01, 2020, *MDPI AG*. doi: 10.3390/mi11100946.

- [58] V. Truxova *et al.*, "Ceramic 3d printing: Comparison of SLA and DLP technologies," *MM Science Journal*, vol. 2020, no. June, pp. 3905–3911, Jun. 2020, doi: 10.17973/MMSJ.2020_06_2020006.
- [59] Z. Jiba *et al.*, "Coating processes towards selective laser sintering of energetic material composites," *Defence Technology*, vol. 16, no. 2, pp. 316–324, Apr. 2020, doi: 10.1016/j.dt.2019.05.013.
- [60] K. Haghsefat and L. Tingting, "FDM 3D Printing Technology and Its Fundemental Properties," *ResearchGate*, 2020, [Online]. Available: https://www.researchgate.net/publication/344768624
- [61] S. Wickramasinghe, T. Do, and P. Tran, "FDM-Based 3D printing of polymer and associated composite: A review on mechanical properties, defects and treatments," Jul. 01, 2020, MDPI AG. doi: 10.3390/polym12071529.
- [62] M. Hikmat, S. Rostam, and Y. Ahmed, "Investigation of tensile property-based Taguchi method of PLA parts fabricated by FDM 3D printing technology," *Results in Engineering*, vol. 11, Sep. 2021, doi: 10.1016/j.rineng.2021.100264.
- [63] R. Patel *et al.*, "A review article on FDM process parameters in 3D printing for composite materials," *Mater Today Proc*, vol. 60, pp. 2162–2166, Jan. 2022, doi: 10.1016/j.matpr.2022.02.385.
- [64] T. Distler *et al.*, "Polymer-Bioactive Glass Composite Filaments for 3D Scaffold Manufacturing by Fused Deposition Modeling: Fabrication and Characterization," *Front Bioeng Biotechnol*, vol. 8, Jun. 2020, doi: 10.3389/fbioe.2020.00552.
- [65] K. Ilyas *et al.*, "Surface Modification of 3D-Printed PCL/BG Composite Scaffolds via Mussel-Inspired Polydopamine and Effective Antibacterial Coatings for Biomedical Applications," *Materials*, vol. 15, no. 23, Dec. 2022, doi: 10.3390/ma15238289.
- [66] T. Kokubo *et al.*, "Solutions able to reproduce in vivo surface-structure changes in bioactive glass-ceramic A-W3."
- [67] A. Moghanian, S. Firoozi, and M. Tahriri, "Characterization, in vitro bioactivity and biological studies of sol-gel synthesized SrO substituted 58S bioactive glass," *Ceram Int*, vol. 43, no. 17, pp. 14880–14890, Dec. 2017, doi: 10.1016/j.ceramint.2017.08.004.
- [68] A. S. Pádua *et al.*, "In Vitro Characterization of Doped Bioglass 45S5/HAp Coatings Obtained by CoBlastTM Deposition," *Coatings*, vol. 13, no. 10, Oct. 2023, doi: 10.3390/coatings13101775.

- [69] Y. Wang *et al.*, "3D printing thermo-responsive shape memory polymer composite based on PCL/TPU blends," *Journal of Polymer Research*, vol. 29, no. 6, Jun. 2022, doi: 10.1007/s10965-022-03095-2.
- [70] K. Phillipson, J. Hay, and M. Jenkins, "Thermal analysis FTIR spectroscopy of poly(ε-caprolactone)," *Thermochim Acta*, vol. 595, pp. 74–82, Nov. 2014, doi: 10.1016/j.tca.2014.08.027.
- [71] J. Oztemur and I. Yalcin-Enis, "Development of biodegradable webs of PLA/PCL blends prepared via electrospinning: Morphological, chemical, and thermal characterization," *J Biomed Mater Res B Appl Biomater*, vol. 109, no. 11, pp. 1844–1856, Nov. 2021, doi: 10.1002/jbm.b.34846.
- [72] M. Queiroz *et al.*, "Does the use of chitosan contribute to oxalate kidney stone formation?," *Mar Drugs*, vol. 13, no. 1, pp. 141–158, Jan. 2015, doi: 10.3390/md13010141.
- [73] M. Pavlovic, "Log-normal Distribution A simple explanation," Towards Data Science. Accessed: Oct. 08, 2024. [Online]. Available: https://towardsdatascience.com/log-normal-distribution-a-simple-explanation-7605864fb67c
- [74] B. Lahcene, "Extended Lognormal Distribution: Properties and Applications," *World Sci News*, Apr. 2020, [Online]. Available: www.worldscientificnews.com
- [75] B. Mahltig and T. Grethe, "High-Performance and Functional Fiber Materials—A Review of Properties, Scanning Electron Microscopy SEM and Electron Dispersive Spectroscopy EDS," Jun. 01, 2022, *Multidisciplinary Digital Publishing Institute (MDPI)*. doi: 10.3390/textiles2020012.
- [76] L. Drummy, J. Yang, and D. Martin, "Low-voltage electron microscopy of polymer and organic molecular thin films," *Ultramicroscopy*, vol. 99, no. 4, pp. 247–256, Jun. 2004, doi: 10.1016/j.ultramic.2004.01.011.
- [77] J. Breedon *et al.*, "Study of polyethylene spherulites using scanning electron microscopy," 1973.
- [78] I. Allan, H. Newman, and M. Wilson, "Antibacterial activity of particulate Bioglass against supra-and subgingival bacteria," 2001.
- [79] S. Paital and N. Dahotre, "Review of laser based biomimetic and bioactive Ca-P coatings," *Materials Science and Technology*, vol. 24, no. 9, pp. 1144–1161, Sep. 2008, doi: 10.1179/174328408X341825.
- [80] K. Haghsefat and L. Tingting, "FDM 3D Printing Technology and Its Fundemental Properties," 2020. [Online]. Available: https://www.researchgate.net/publication/344768624

A PRINTED STRUCTURS

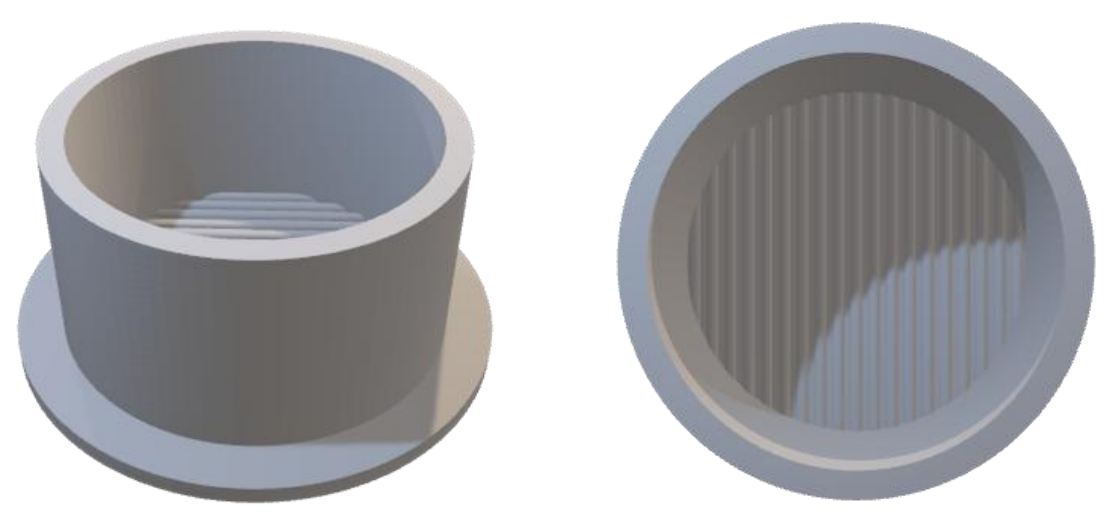


Figure A.1 - 3D model of the structure for cell-based tests





Figure A.2 - Printed structures for cell-based tests



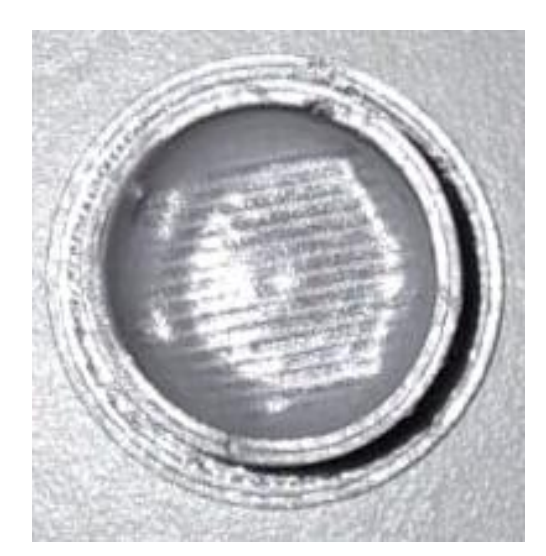


Figure A.3 - Printed structures for cell-based tests with coating



Manuel Macedo